


First-principles study of excitons in optical spectra of silver chlorideArnaud Lorin,^{1,2} Matteo Gatti,^{1,2,3} Lucia Reining^{1,2} , and Francesco Sottile^{1,2}¹*LSI, CNRS, CEA/DRF/IRAMIS, École Polytechnique, Institut Polytechnique de Paris, F-91120 Palaiseau, France*²*European Theoretical Spectroscopy Facility (ETSF)*³*Synchrotron SOLEIL, L'Orme des Merisiers, Saint-Aubin, BP 48, F-91192 Gif-sur-Yvette, France*

(Received 15 September 2020; revised 27 September 2021; accepted 29 November 2021; published 23 December 2021)

Silver chloride is a material that has been investigated and used for many decades. Of particular interest are its optical properties, but only few fundamental theoretical studies exist. We present first-principles results for the optical properties of AgCl, obtained using time-dependent density functional theory and many-body perturbation theory. We show that optical properties exhibit strong excitonic effects, which are correctly captured only by solving the Bethe-Salpeter equation starting from quasiparticle self-consistent *GW* results. Numerical simulations are made feasible by using a model screening for the electron-hole interaction in a way that avoids the calculation of the static dielectric constant. Finally, the localization of bright and dark excitons is discussed.

DOI: [10.1103/PhysRevB.104.235149](https://doi.org/10.1103/PhysRevB.104.235149)**I. INTRODUCTION**

Silver chloride is a versatile material, long known for a large variety of applications. For instance, it is a reference electrode for electrochemical measurements [1], and in its nanostructured phase it has remarkable antimicrobial properties [2–4]. Moreover, it has been recently shown that silver clusters at AgCl surfaces form an efficient photocatalytic system [5–9]. The largest range of applications of AgCl is related to its optical properties: it is responsible for several shades in stained glass [10], and it is widely used as photochromic material in photosensitive glasses [11]. In particular, AgCl is a crucial ingredient in photographic paper to produce the latent image [12,13]. It was already the key component in the first color photography in history realized by Becquerel in 1848 [14]: a recent study has shown that the colors in Becquerel's photochromatic images were due to silver nanoparticles in a silver chloride matrix [15–17].

In spite of the importance of its optical properties, experimental results, including absorption, reflectivity, and luminescence, are relatively old [18–29] (see Refs. [30,31] for more recent reviews). Moreover, the same photochromic properties of AgCl that make it so appealing for applications also hamper spectroscopy experiments: its electronic and optical properties can be changed significantly by irradiation with light [32], thus affecting the reliability of the measured spectra. On the other side, theoretical simulations are a valuable tool to provide a solid benchmark and remove possible ambiguities from experimental results. Several first-principles studies [33–39] within density functional theory [40,41] (DFT) have focused on ground-state properties and the Kohn-Sham electronic structure. However, these methods cannot access the band gap, a fundamental ingredient for the optical properties. Only recently, band-structure calculations using the *GW* approximation [42] (GWA) within many-body perturbation theory [43] (MBPT) have yielded more reliable

numbers for the photoemission gaps [44–46]. Instead, to the best of our knowledge, MBPT studies for the optical properties of silver chloride are still missing.

This work aims at bridging this gap: we have conducted state-of-the-art electronic structure calculations to investigate the optical properties of bulk AgCl. Indeed, aside from its strong interest for a wide range of applications, AgCl is challenging from the theoretical point of view: Ag *4d* states are strongly hybridized with Cl *3p* and have a direct impact on the band gap. Their strong localization requires a high cutoff in plane-wave calculations, and it moreover poses problems for simple density functionals such as the local density approximation (LDA) or the generalized gradient approximation (GGA). Simple models [47,48] are not reliable because of its peculiar band structure and estimates of excitonic effects based on the Wannier model (see, e.g., Refs. [30,31]) should be examined with great care: advanced first-principles approaches are needed in order to get reliable insight.

The questions that we will address in this work are the following: Which level of theory is needed for a proper description of optical properties of AgCl, including questions related to pseudopotentials, self-consistency, and excitonic effects? Can we simplify the calculations, in spite of the complexity of the material? How strong are excitonic effects due to the electron-hole interaction? Finally, *the nature of excitons* in AgCl is a crucial question with a direct impact on all the applications that involve the optoelectronic properties of AgCl.

Section II summarizes the approaches used to access ground- and excited-state properties. Results for the band structures from DFT and MBPT, as well as first results for the optical properties, are given in Sec. III. In Sec. IV, we propose a way to efficiently use a model screening of the electron-hole interaction, and we show that this allows us to overcome the computational limitations and obtain reliable optical spectra. Finally, Sec. V is dedicated to the discussion of excitonic

effects in the optical properties of AgCl, and conclusions are drawn in Sec. VI.

II. METHODOLOGY

Starting from a DFT ground-state calculation, there are two possible routes to determine optical spectra [49]: first, to extend DFT to time-dependent DFT [50,51] (TDDFT), and second, to move to MBPT [43,52], where the one-body Green's function is determined from a Dyson equation with a given approximation for the self-energy, and subsequently optical properties are derived from the solution of a Bethe-Salpeter equation [53,54] (BSE) for the two-body correlation function. When simple approximation for the exchange-correlation (xc) functionals are sufficient, TDDFT is computationally more efficient than MBPT. It is therefore interesting to compare the results of the two approaches, and we will detail both routes in the following. Atomic units are used in this paper.

A. Optical absorption with time-dependent density functional theory

The optical properties of a system are linked to the inverse dielectric function $\epsilon^{-1} = 1 + v_c \chi$, where v_c is the Coulomb potential and χ is the linear density-density response function. This quantity can be accessed, in principle exactly, using TDDFT in linear response [55]. First, one has to build the noninteracting polarizability χ^0 on the basis of Kohn-Sham (KS) DFT ingredients.

The full density-density response function χ is then obtained from the Dyson-type linear-response equation [55]

$$\chi = \chi^0 + \chi^0(v_c + f_{xc})\chi, \quad (1)$$

where in reciprocal space all quantities are functions of momentum \mathbf{q} in the first Brillouin zone and (aside from v_c) of ω , and matrices in reciprocal-lattice vectors \mathbf{G}, \mathbf{G}' . The exchange-correlation kernel, that in real-space and real-time reads as $f_{xc}(\mathbf{r}, \mathbf{r}', t - t') \equiv \delta v_{xc}(\mathbf{r}, t) / \delta n(\mathbf{r}', t')$, is the functional derivative of the xc potential with respect to the density n . It depends on two space (or reciprocal space) arguments and on the time difference $t - t'$ (or frequency ω). Its exact expression is unknown. Two extensively used approximations are the random-phase approximation (RPA) $f_{xc} \approx 0$, and the adiabatic local density approximation (ALDA), where $f_{xc}(\mathbf{r}, \mathbf{r}', t - t') \approx \delta(\mathbf{r} - \mathbf{r}')\delta(t - t')dv_{xc}^{\text{LDA}}/dn|_{n(\mathbf{r},t)}$. From the density-density response function we evaluate the inverse dielectric function

$$\epsilon_{\mathbf{G}, \mathbf{G}'}^{-1}(\mathbf{q}, \omega) = \delta_{\mathbf{G}, \mathbf{G}'} + \frac{4\pi}{|\mathbf{q} + \mathbf{G}'|^2} \chi_{\mathbf{G}, \mathbf{G}'}(\mathbf{q}, \omega). \quad (2)$$

The macroscopic dielectric function [56,57] is then

$$\epsilon_M(\omega) = \lim_{\mathbf{q} \rightarrow 0} \frac{1}{\epsilon_{\mathbf{G}=\mathbf{G}'=0}^{-1}(\mathbf{q}, \omega)}. \quad (3)$$

From the macroscopic dielectric function we derive optical properties: optical absorption is related to the imaginary part, $\text{Im} \epsilon_M$, and the extinction coefficient is given by $\kappa = \text{Im} \sqrt{\epsilon_M}$. For optical properties, the wave vector is very small compared to the crystal, and we take the limit $\mathbf{q} \rightarrow 0$ (where the

transverse and longitudinal dielectric functions coincide [58]). Equation (3) takes into account crystal local field effects because the dielectric matrix is inverted before the macroscopic average $\mathbf{G} = \mathbf{G}' = 0$ is taken.

B. Band structure with the GW approximation

KS eigenvalues cannot be interpreted as electron removal and addition energies, but they often give a good overview of the band structure and constitute a convenient starting point for further calculations. In order to obtain a more meaningful band structure, we add quasiparticle corrections using the Green's function formalism. In the quasiparticle approximation, addition and removal energies are obtained from a modified one-particle equation [42,52]

$$\left[-\frac{1}{2} \nabla^2 + v^{\text{ext}}(\mathbf{r}) + v_H(\mathbf{r}) \right] \phi_{n\mathbf{k}}(\mathbf{r}) + \int d\mathbf{r}' \Sigma_{xc}(\mathbf{r}, \mathbf{r}', E_{n\mathbf{k}}) \phi_{n\mathbf{k}}(\mathbf{r}') = E_{n\mathbf{k}} \phi_{n\mathbf{k}}(\mathbf{r}), \quad (4)$$

where, aside from the external and Hartree potentials v^{ext} and v_H , the self-energy Σ_{xc} plays the role of an effective nonlocal and energy-dependent potential. The generalized eigenvalues of Eq. (4) can be interpreted as addition and removal energies, and are used to build the theoretical band structure. The quasiparticle wave functions $\phi_{n\mathbf{k}}$ are also in principle different from the KS ones, which changes in particular the density. A widely used approximation for the self-energy is Hedin's GWA [42]. In this approximation, $\Sigma_{xc} = iGW$ is the product of the one-body Green's function G and the screened Coulomb interaction $W = \epsilon^{-1}v_c$.

The G^0W^0 approach [59–62] replaces the Green's function entering the self-energy by the KS one and evaluates the screened Coulomb interaction W using the RPA for ϵ^{-1} following Eq. (1). A further simplification is obtained by evaluating the quasiparticle eigenvalues perturbatively with respect to the KS ones, and by making use of the fact that the self-energy is approximately linear around the quasiparticle energy. This yields

$$E_{n\mathbf{k}} = \varepsilon_{n\mathbf{k}} + Z_{n\mathbf{k}}[\langle \Sigma_{xc}(\varepsilon_{n\mathbf{k}}) \rangle - \langle v_{xc} \rangle], \quad (5)$$

with $\varepsilon_{n\mathbf{k}}$ the KS eigenvalue, v_{xc} the KS xc potential, and the quasiparticle renormalization factor $Z_{n\mathbf{k}} = [1 - \langle \frac{\partial \Sigma_{xc}(\omega)}{\partial \omega} |_{\varepsilon_{n\mathbf{k}}} \rangle]^{-1}$. Here, expectation values are taken with the KS wave functions. The G^0W^0 approach based on KS calculations with approximate functionals such as the LDA or GGA has met broad success for many materials [52,61–63], but it encounters problems when it comes to materials with localized electrons [52,63–67]. These are often transition metal oxides and other correlated materials where d or f electrons are important, but as we will see, the problem also concerns AgCl, because of the hybridization between Ag $4d$ and Cl $3p$ electrons. These materials require better starting eigenvalues and wave functions, or self-consistency. A prominent self-consistent approach is quasiparticle self-consistent GW [64,65] (QS GW). In this approach, Eq. (4) is approximated by an effective Schrödinger equation with a static Hamiltonian, and the resulting eigenvalues and eigenfunctions are used to build a new quasiparticle Green's function and screened

Coulomb interaction. The procedure can be iterated to self-consistency and often improves over G^0W^0 results [52,63–67]. One delicate point in the evaluation of the GW self-energy is frequency integration. Since Σ_{xc} is a product of G and W in real space and time, it becomes a convolution in frequency space. We have performed the frequency integration using the Godby-Needs plasmon-pole model (PPM) [68] and we have validated the PPM results with respect to those obtained with the accurate contour deformation technique [69].

C. Optical absorption with the Bethe-Salpeter equation

The electron addition and removal quasiparticle band structure obtained from the GW calculation can be used as starting point to determine the linear-response properties in the framework of MBPT, as an alternative to TDDFT. The density-density response function χ is linked to the two-particle correlation function L by the relation $\chi(\mathbf{r}_1, \mathbf{r}_2; t_1 - t_2) = -iL(\mathbf{r}_1, t_1, \mathbf{r}_1, t_1, \mathbf{r}_2, t_2, \mathbf{r}_2, t_2)$. L , in turn, can be obtained from the solution of the BSE [53,54]. In the GWA and neglecting variations of the screening upon perturbation of the system this equation reads as

$$L(1, 2, 3, 4) = L^0(1, 2, 3, 4) + L^0(1, 2, \bar{5}, \bar{6})[v_c(\bar{5}, \bar{7})\delta(\bar{5}, \bar{6})\delta(\bar{7}, \bar{8}) - W(\bar{5}, \bar{6})\delta(\bar{5}, \bar{7})\delta(\bar{6}, \bar{8})]L(\bar{7}, \bar{8}, 3, 4). \quad (6)$$

Here, (1) is a shorthand notation for position, time, and spin $(\mathbf{r}_1, t_1, \sigma_1)$, barred indices are integrated over. $L^0(1, 2, 3, 4) = G(1, 3)G(4, 2)$ is the two-particle correlation function in absence of interaction between the two particles, and W is the screened Coulomb interaction calculated within RPA. As before, we will not consider spin in the following. As a further approximation, usually the quasiparticle approximation is made for G in L_0 and the frequency dependence of W is neglected in the kernel of the BSE. In this case, one can immediately set $t_1 = t_4$ and $t_2 = t_3$ in Eq. (6), and the resulting equation can be reformulated as an eigenvalue problem with an effective electron-hole Hamiltonian H_{exc} , where v_c and W show up as effective electron-hole interactions [49,70–72]. This Hamiltonian is usually expressed in a basis of pairs of orbitals. In systems with a gap at zero temperature, only pairs of an occupied and an unoccupied orbital contribute to the absorption spectrum, so the pair corresponds to a transition $|t\rangle$. In this basis the Hamiltonian reads as

$$\langle t|H_{exc}|t'\rangle = E_t\delta_{t,t'} + \langle t|K|t'\rangle, \quad (7)$$

where the energy E_t is the difference between an unoccupied and an occupied quasiparticle state, calculated in the GWA, and the kernel K is the sum of the electron-hole interactions: $K = v_c - W$. $E_t > 0$ (< 0) for resonant (antiresonant) transitions.

The Tamm-Dancoff approximation [73,74] (TDA) neglects the coupling between resonant and antiresonant transitions. It is usually a good approximation for absorption spectra of solids. We have verified that this is also true for AgCl, and all results shown in the following are obtained within the TDA.

The macroscopic dielectric function from the solution of the BSE, taking into account local field effects [49], can be

calculated directly in the TDA as

$$\epsilon_M(\omega) = 1 - \lim_{q \rightarrow 0} \frac{8\pi}{N_k \Omega_0 q^2} \sum_{\lambda} \frac{|\sum_t A_{\lambda}^t \tilde{\rho}_t(\mathbf{q})|^2}{\omega - E_{\lambda} + i\eta}, \quad (8)$$

where the oscillator strengths $\tilde{\rho}_t(\mathbf{q}) \equiv \tilde{\rho}_{n_1 n_2 \mathbf{k}}(\mathbf{q}) = \int \psi_{n_1 \mathbf{k}-\mathbf{q}}^*(\mathbf{r}) e^{-i\mathbf{q}\cdot\mathbf{r}} \psi_{n_2 \mathbf{k}}(\mathbf{r}) d\mathbf{r}$, while A_{λ} and E_{λ} are solutions of a modified H_{exc} , where the bare Coulomb interaction v_c of the electron-hole exchange does not have its long-range component $v_c(\mathbf{G} = 0)$; note that the sets of E_{λ} contain both positive and negative energies. They can be different from the independent-(quasi)particle transition energies E_t . If the exciton energy E_{λ} is smaller than the direct gap (i.e., the smallest E_t), then the exciton is said to be bound and the difference $E_t - E_{\lambda}$ is its binding energy. The coefficients A_{λ} mix the previously independent transitions contained in $\tilde{\rho}$. This suggests to analyze spectra in terms of the independent transitions that contribute to a given many-body transition λ . The eigenvectors of the excitonic Hamiltonian $|A_{\lambda}^t|^2$ as a function of t or E_t indicate how much each transition between an occupied and an empty state is mixed into the excitonic eigenstate λ . The electron-hole correlation in real space can be examined by investigating the e - h wave function,

$$\Psi_{\lambda}(\mathbf{r}_h, \mathbf{r}_e) = \sum_{t=v_c \mathbf{k}} A_{\lambda}^t \phi_{v\mathbf{k}}^*(\mathbf{r}_h) \phi_{c\mathbf{k}}(\mathbf{r}_e). \quad (9)$$

In particular, one can fix the position $\mathbf{r}_h = \mathbf{r}_h^0$ of the hole and visualize the corresponding density distribution of the electron, $n_{\lambda}(\mathbf{r}_e) = |\Psi_{\lambda}(\mathbf{r}_h^0, \mathbf{r}_e)|^2$, for a given exciton λ .

Finally, we introduce the cumulative sums

$$I_{\lambda}(\omega) = \lim_{q \rightarrow 0} \sqrt{\frac{8\pi}{N_k \Omega_0 q^2}} \sum_t^{E_t < \omega} A_{\lambda}^t \tilde{\rho}_t(\mathbf{q}) \quad (10)$$

and

$$S_{\lambda}(\omega) = |I_{\lambda}(\omega)|^2. \quad (11)$$

Since in the sum there can be both constructive or destructive interference effects between the complex numbers A_{λ}^t and $\tilde{\rho}_t$, the cumulative sum is not necessarily a monotonous function. The value of $S_{\lambda}(\omega \rightarrow \infty)$ gives the oscillator strength with which an exciton λ contributes to the absorption spectrum [see Eq. (8)]. If it is negligibly small, the exciton is said to be dark. Otherwise, if it has a significant contribution to the absorption spectrum the exciton is called bright.

III. RESULTS

A. Kohn-Sham band structure

AgCl crystallizes in the fcc rocksalt structure. Calculations are carried out at the room-temperature experimental lattice constant [75,76] $a_{\text{expt}} = 5.55 \text{ \AA}$.

The Kohn-Sham band structure in the LDA is shown in Fig. 1. With the top valence at L and the bottom conduction at Γ , the minimum gap is indirect and amounts to 0.56 eV. The minimum direct gap lies close to Γ , at about $\frac{2}{9} \Gamma - K$, followed by a direct gap at $\frac{1}{6} \Gamma - X$ and the direct gap at Γ ; these gaps are 2.78, 2.85, and 2.86 eV, respectively. These values are consistent with previous LDA calculations [33,34,37–39,45]. In GGA the indirect $L \rightarrow \Gamma$ gap is 0.3 eV larger [34–37,44,46].

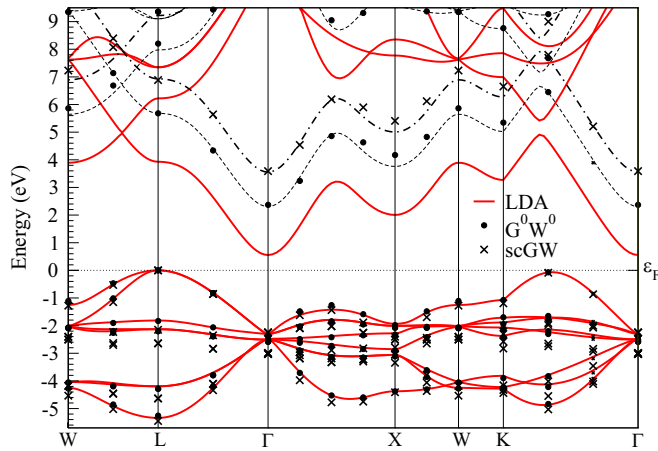


FIG. 1. Calculated band structure of silver chloride. The top valence energy has been aligned to zero in all cases. Red lines are the LDA calculation, the dots the G^0W^0 results, and the crosses the QSGW results. The dashed and dotted-dashed lines represent the conduction bands shifted from the LDA by 1.9 and 2.98 eV, respectively.

Since, to the best of our knowledge, inverse photoemission spectra are not available for AgCl, the fundamental gaps have been extracted from optical measurements [31] and resonant Raman scattering experiments [30,77]. The onset of the lowest-energy peak in the absorption spectrum gives an estimation of the minimum direct gap. The tail of the peak extending towards low energies is due to phonon-assisted absorption processes [30,31]: its edge can be used to infer the value of the indirect gap. However, in both cases one also has to take into account the fact that the photoemission gap is larger than the absorption peak position by the exciton binding energy, whose estimation can introduce uncertainties in the band-gap value. We will come back to this point in Sec. V. In any case, the KS gaps severely underestimate the experimental values of 5.13 eV for the direct optical gap [25], and 3.25 eV for the indirect absorption edge [23,77].

Earlier theoretical studies [30,31,47,78,79] have found that $\text{Ag}^+ 4d$ and $\text{Cl}^- 3p$ ionic states have similar energy in the crystal, leading to strong hybridization in the valence band. While their mixing is zero at Γ , it is strong elsewhere, notably at L . This \mathbf{k} -dependent hybridization and the strong $p-d$ repulsion cause the upward curvature of the top valence bands at Γ (i.e., a negative hole effective mass) and make AgCl an indirect semiconductor. On the contrary, in the alkali-metal halides, which share the same rocksalt crystal structure, the ionic energy levels are well separated, leading to a much larger ionic character of the compounds and a direct band gap.

Our calculations, as shown by the band structure in Fig. 1 and the projected density of states (PDOS) in Fig. 2, confirm this picture. While Cl $3s$ states are located at ~ -15 eV (not shown), the valence band region comprises eight bands. They are very close to each other at the Γ point, where from the bottom to the top we count three degenerate Ag t_{2g} states,¹ two degenerate Ag e_g states, and three degenerate Cl $3p$ states.

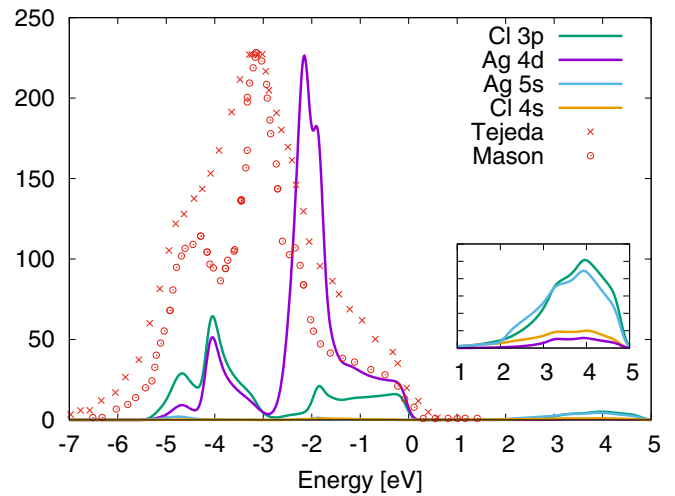


FIG. 2. Projected density of states of silver chloride calculated in KS-LDA compared to photoemission spectra from Mason [80] and Tejada *et al.* [78] at a photon energy $h\nu = 1486.6$ eV. In each curve the top valence has been aligned to zero and the intensity scaled to the maximum of the most prominent peak. In the inset: zoom on the calculated unoccupied PDOS.

The hybridization between Ag $4d$ and Cl $3p$ increases moving away from the Γ point towards the top and the bottom of the valence bands at the L point, where Ag $4d$ and Cl $3p$ are strongly mixed. Their interaction gives rise to dispersive bands. Instead, three Ag $4d$ bands, which are not dispersive between Γ and L , remain at the center of the valence manifold, giving rise to a pronounced sharp peak in the PDOS. Finally, the lowest conduction band has a delocalized Ag $5s$ and Cl $4s$ character at the Γ point [38] and mixed Ag $5s$ -Cl $3p$ elsewhere.

In Fig. 2 the calculated PDOS is compared to experimental photoemission spectra measured at 1486.6 eV photon energy by Mason [80] and Tejada *et al.* [78]. The two measured spectra, taken at the same photon energy, differ in their shapes, illustrating the experimental difficulty of the characterization of the electronic properties of AgCl. Still we can analyze their common features. The measured spectra are characterized by a bandwidth of about 6 eV and a main peak centered at about -3.1 eV. The calculation correctly describes the presence of shoulders about 4 eV below the main peak and about 2 eV above it. On the basis of atomic photoionization cross sections [81], we find that photoemission spectra at $h\nu = 1486.6$ eV mostly probe the Ag $4d$ electrons. We can therefore directly compare the experimental spectra to the calculated Ag $4d$ PDOS. We thus assign the main peak to the nondispersive Ag $4d$ bands, which result too shallow by about 1 eV in KS-LDA. This underestimation of the binding energy of occupied localized d levels is a common tendency of KS-LDA that can be improved by the GWA (see, e.g., [63,82–86]), as we will discuss more in detail in the next subsection.

B. Band structure in the GW approximation

The band structure of silver chloride evaluated in G^0W^0 has been added to the KS-LDA band structure in Fig. 1. The top of the valence band is aligned to zero. The G^0W^0 band structure

¹The crystal field at Ag site has a cubic point symmetry (O_h).

TABLE I. Direct and indirect photoemission gaps from different approximations compared to experimental (Expt.) absorption onsets from optical measurements (Refs. [23,25]) which provide a lower bound due to excitonic effects (see Sec. V).

	Indirect	Direct
LDA	0.56	2.78
G^0W^0 (PPM)	2.4	4.8
G^0W^0 (CD)	2.4	4.6
G^0W^0 (EET)	2.4	4.7
QSGW	3.7	5.9
evQSGW	3.2	5.7
Absorption onset (Expt.)	3.25	5.13

is similar to the KS-LDA one, aside from an almost rigid shift of 1.8–1.9 eV of the conduction bands. For illustration, the dashed curve shows the lowest conduction bands in KS-LDA, shifted upwards by 1.9 eV.

This size of the band-gap opening is in agreement with the value of 1.75 eV recently obtained by Zhang and Jiang [46] in a G^0W^0 full-potential linearized augmented plane-wave calculation starting from a KS-GGA band structure. Instead, van Setten *et al.* [44] reported a much smaller G^0W^0 correction to the KS-GGA gap: 1.25 eV. The reason of this large discrepancy should not be ascribed to inaccuracies in the pseudopotentials [46], but rather to an underconvergence problem: their automatized algorithm employed only 155 bands (compared to 820 in this work). On the contrary, Gao *et al.* [45] found a much larger G^0W^0 correction starting from KS-LDA, i.e., 2.38 eV, and had to include up to 2500 empty bands in the G^0W^0 calculation. A similar situation was previously encountered in other materials like ZnO [87–89] and TiO₂ [90], where semicore electrons have to be explicitly included in the GW calculation. The origin of the problem in those calculations was identified [89,90] with the use of the f -sum rule in the Hybertsen-Louie [59] PPM, which was adopted also by Ref. [45] for AgCl. An alternative PPM proposed by Godby and Needs [68], which is instead optimized for the spectral range of interest, does not create this problem. Also in the present case, our results obtained with the Godby-Needs PPM agree (within 0.2 eV at most) with the accurate contour-deformation (CD) calculation that we have carried out as benchmark (see Table I). As a final validation, we have also employed the effective energy technique [91] (EET) that accounts approximately for all empty states and allows reaching convergence much more easily than the traditional sum-over-states scheme. Using the EET (here used within the PPM) the values for the band gaps are once again in agreement within 0.1 eV (see Table I).

Our G^0W^0 indirect band gap is 2.4 eV and the direct gap at Γ is 4.6–4.8 eV. Both are still smaller than the experimental optical gaps (see Table I). However, in situations with large pd hybridization as for AgCl the LDA starting point may not be reliable [65]. Moreover, the large corrections obtained within the G^0W^0 scheme question the first-order perturbative approach itself.

In order to overcome the problem of the KS-LDA starting point and assess the G^0W^0 perturbative scheme, we have performed QSGW calculations. The new band structure is shown in Fig. 1; again, top valence bands are aligned. At first sight, there is no drastic change in the dispersion of the

valence and conduction bands. However, a closer look at Fig. 3 allows for a more detailed analysis. Figure 3 displays the QP energy corrections obtained within the QSGW scheme as a function of the corresponding KS-LDA energies. There, both the horizontal and vertical axes have been aligned to zero for the top valence state at L . Whereas the G^0W^0 valence bands were essentially on top of the KS-LDA ones, QSGW results slightly increase, by 0.1 eV, the valence bandwidth and push the narrow Ag $4d$ bands in the middle of the valence band down by 0.5 eV, leading to a better agreement with photoemission results [78,80]. The remaining 0.5-eV discrepancy is similar to what is observed for shallow d levels in other semiconductors: for further improvement, vertex corrections in the self-energy beyond the GWA should be included [86]. The most obvious change is the almost rigid shift of the conduction bands with respect to KS-LDA, which has passed from 1.9 eV in G^0W^0 to 2.98 eV, as indicated by the dotted-dashed line in Fig. 1 and the horizontal blue line in Fig. 3. With this shift, the indirect gap becomes 3.7 eV while the direct band gap is 5.9 eV. The fact that now band gaps seem to be overestimated (see Table I) may have two reasons. First, the self-consistent RPA screening in QSGW is too weak, which brings results too close to Hartree-Fock [52,65,67,85,92]. The inclusion of the attractive electron-hole interaction, i.e.,

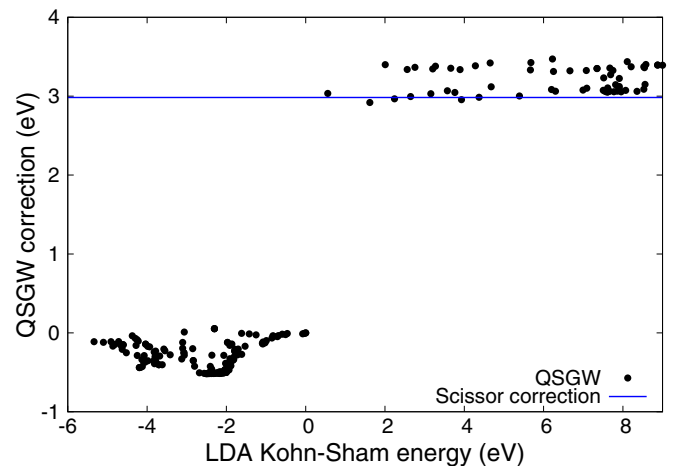


FIG. 3. QSGW QP energy corrections as a function of the corresponding KS-LDA energies. The corrections have been set to zero for the top valence state, whose KS-LDA energy is also set to zero. The horizontal blue line is the value of the scissor correction used in the calculation of absorption spectra in Sec. V A.

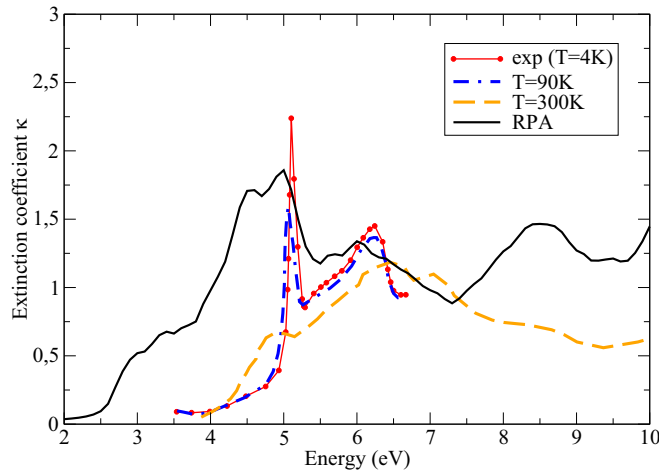


FIG. 4. Extinction coefficient as a function of energy. The RPA calculation based on the KS-LDA band structure (black solid curve) is compared to experimental data from Ref. [25] measured at 4 K (red curve), at 90 K (blue curve), and at room temperature (orange curve).

a vertex correction, in the screened interaction W has been shown to improve QSGW band gaps of semiconductors [52,92]. Moreover, the electron-phonon interaction, here neglected, also leads to a band-gap renormalization [93–96]. Second, the experimental optical gaps may be affected by excitonic effects, which is the topic of this work (see Sec. V).

Finally, Fig. 3 shows that the QSGW corrections for the conduction bands are grouped around two main values: aside from the 2.98-eV shift corresponding to the band gap opening around Γ , a second group of states undergo a larger correction of 3.35 eV. The latter stems from the bottom conduction band between X , W , and K .

We have also performed a QSGW calculation where only the QP eigenvalues are calculated self-consistently, while the QP wave functions are constrained to remain the KS-LDA orbitals. This further calculation is named “evQSGW” in Table I. It gives band gaps that are intermediate between the G^0W^0 and the full QSGW results, illustrating the impact of the change of the wave functions on the band structure. Finally, we have tested the effect of the update of the screened Coulomb interaction W : a QSGW calculation, in which we keep W fixed at the level of the RPA-LDA W_0 , yields gaps (direct 4.8 eV and indirect 2.7 eV) that are closer to the G^0W^0 ones than to the QSGW results. In the QSGW calculation in AgCl the modification of the screened interaction W is hence the most critical effect.

C. Absorption spectra

Since the optical properties of AgCl are of utmost importance for its applications, their calculation and analysis represents the focus of this work.

1. Absorption spectrum in time-dependent density functional theory

Figure 4 shows the extinction coefficient $\kappa(\omega)$. We compare the RPA result (black curve) with three representative experiments at different temperatures: 4 K (red curve), 90 K

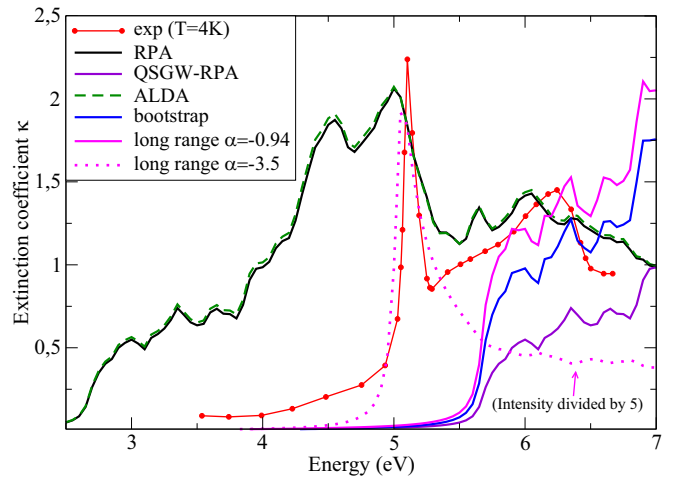


FIG. 5. Comparison of the extinction coefficient measured at 4 K with several TDDFT approximations. Since the energy range is limited to 3–7 eV, these spectra have been calculated with only four conduction bands.

(blue curve), 300 K (orange curve). The spectra in Fig. 4 have been measured up to 6.7 eV in Ref. [25]. The wider range at room temperature has been obtained by combining results from different sources in Ref. [25]. The measured spectra are highly sensitive to the experimental conditions. In Sec. V A we will come back to this point by comparing the 4-K spectrum with another low-temperature experimental result from Ref. [31]. Here we can already notice how the shape of the measured spectra is strongly affected by temperature: the very sharp peak at the onset of the spectrum around 5.1 eV is clearly visible only at low temperatures, while the room-temperature spectrum is much broader. Since our calculations do not include the effect of temperature, comparison to the low-temperature experiment should be more meaningful. Still, keeping this fact in mind, also the room-temperature experiment gives important indications. Overall, the RPA and experimental spectrum at 300 K are similar. However, the absorption onset is underestimated in the RPA, by more than 1 eV. Moreover, the RPA entirely misses the sharp feature at the onset of the low-temperature experimental result. The underestimate of the onset is a common problem in KS-RPA spectra [49]. Since $f_{xc} = 0$ and only short-range components of v_c contribute to optical spectra, the onset is determined by the interband transitions in χ_0 . It suffers therefore both from the use of the LDA, and from the fact that even the exact KS band gap would be smaller than the measured band gap. The results do not change when f_{xc} is taken into account within the ALDA: in Fig. 5 the ALDA (dashed green curve) is hardly distinguishable from the RPA (black curve). The ALDA can neither lead to a significant opening of the optical gap, nor to a significant change in the spectral shape.

It is well established [97,98] that the ALDA suffers from the absence of a long-range contribution that in nonzero-band-gap materials would diverge as $1/q^2$ for the large wavelength of the light, $q \rightarrow 0$. The exact xc kernel should contain such a contribution. Several suggestions exist how to include a long-range component in f_{xc} [98–101]. All kernels of this family start from a χ_0 built with a quasiparticle band structure from

GW or similar approaches, instead from a KS one. A simple static and scalar f_{xc} with a long-range contribution can then simulate the effects of the electron-hole interaction by shifting spectral weight to lower energies.

In order to simulate the missing excitonic effects, we have examined the long-range kernel [98] of the type α/q^2 , where the band-gap opening at the QSGW level is accounted for by a scissor correction of 2.98 eV. The result is given by the pink curve in Fig. 5. The value of $\alpha = -0.94$ has been obtained from Eq. (4) of Ref. [99] using an experimental dielectric constant $\epsilon_\infty = 4$ [102,103]. In contrast to the ALDA, the long-range kernel does shift the spectral weight to lower energies with respect to the QSGW+RPA result (violet curve), where $f_{xc} = 0$. However, the spectral onset remains at the QSGW one, overestimating the experimental result, and the sharp peak is still missing. A larger value of $|\alpha|$ in the long-range kernel α/q^2 would enhance the excitonic effects. However, in order to reproduce the sharp experimental peak, we should increase the strength $|\alpha|$ to very large values, which leads to a very bad spectral shape. For example, the dotted curve in Fig. 5 is obtained with $\alpha = -3.5$. Note that for the figure its overall intensity is divided by a factor 5 since the peak at the onset is now much too strong, while all other spectral features are flattened. This failure of static long-range kernels is confirmed also by similar approaches, such as the recent bootstrap kernel [104,105] [see the blue curve in Fig. 5, obtained by using Eq. (5) of Ref. [105]]. Therefore, we can conclude that TDDFT with the presently available simple approximations does not give a good description of the optical properties of AgCl, and in particular, of the strong excitonic effects that should explain the remaining discrepancy between theory and experiment. For this reason, we have to move on to a full description in the framework of MBPT, by solving the BSE.

2. Optical spectra from the Bethe-Salpeter equation: Insight and difficulties

A state-of-the art BSE calculation starts from the G_0W_0 band structure (here simulated by a scissor shift of 1.9 eV) and employs the LDA-RPA screened Coulomb interaction W to account for the electron-hole attraction. The result of a G_0W_0 -BSE calculation obtained with 2048 shifted [106] \mathbf{k} points and 19 bands is shown in Fig. 6. This kind of calculation is computationally expensive. A \mathbf{k} -point convergence test performed with a reduced number of conduction bands indeed shows that at least 2048 shifted \mathbf{k} points should be used [we have tested up to 6912 shifted \mathbf{k} points (see Fig. 17 in Appendix)]. The need for a quite large number of \mathbf{k} points is related to the particular band structure of AgCl: the smallest direct gap is located at \mathbf{k} points that are not high-symmetry points (see Sec. III A). A homogeneous \mathbf{k} -point grid that includes these \mathbf{k} points must be very dense.

The G_0W_0 -RPA onset of the spectrum (pink dashed line in Fig. 6) underestimates the experimental threshold and does not show a pronounced peak at low energy: it merely shifts the LDA-RPA spectrum to higher energy. The electron-hole interaction in the BSE shifts oscillator strength to lower energies, and a peak forms (black lines in Fig. 6). However, the G_0W_0 +BSE spectrum is now at an even lower energy and the excitonic peak is much too weak with respect to experiment.

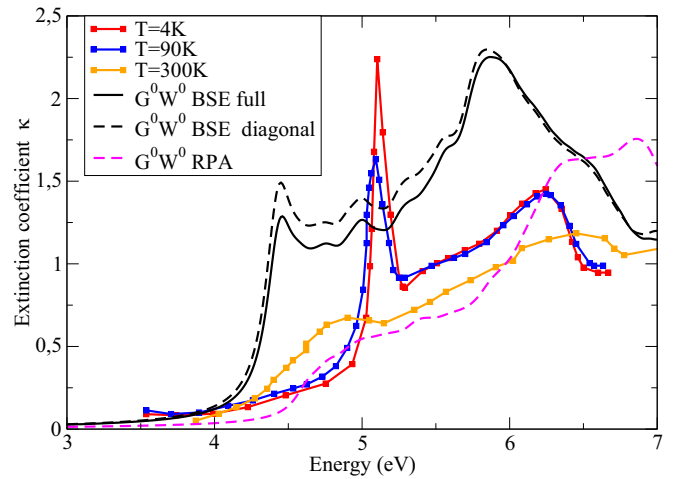


FIG. 6. Comparison between the experimental extinction coefficient from Ref. [25] at different temperatures and MBPT calculations (with 2048 shifted \mathbf{k} points and 19 bands): G_0W_0 -RPA obtained with 1.9-eV scissor correction (pink dashed line) G_0W_0 +BSE obtained with the full screening matrix $W_{GG'}(\mathbf{q})$ (black solid line) or only its diagonal contribution (black dashed line).

BSE calculations in solids are often done by neglecting the off-diagonal elements of the screening matrix [49,71] $W_{GG'}(\mathbf{q})$ that represents the direct electron-hole interaction. We note that this does not imply neglecting local field effects altogether since they are accounted for by the modified bare Coulomb interaction in the electron-hole exchange. The diagonal approximation to W is justified when the electron-hole pair is delocalized enough to justify a space-averaged screening. The first excitonic peak in AgCl is influenced by this approximation: taking into account the full spatial details of screening (solid black line in Fig. 6) reduces the peak intensity by about 10% with respect to the approximation of diagonal screening (dashed black line in Fig. 6).

This G_0W_0 +BSE calculation remains qualitative for several reasons. As pointed out above, the G_0W_0 band structure from an LDA starting point is not reliable for AgCl. While this issue could be solved by using the QSGW band structure as a starting point for the BSE calculation, the main computational problem would still remain the setting up of the full screening matrix $W_{GG'}(\mathbf{q})$ that should be calculated self-consistently for too many \mathbf{q} points. In order to overcome this problem, we complement the first-principles calculations with a model screening, where the parameters of the model are fitted to the *ab initio* results. As we will see in the next section, a careful analysis allows us to turn this simple approach into a powerful way to obtain reliable results. We also note that the assessment of this model screening approach has a relevance that goes beyond AgCl itself, as the same method could be efficiently applied to more complex materials, making very expensive calculations possible.

IV. MODEL SCREENING OF THE ELECTRON-HOLE INTERACTION

The screened Coulomb interaction is evaluated in Fourier space as

$$W_{GG'}(\tilde{\mathbf{q}}) = \epsilon_{GG'}^{-1}(\tilde{\mathbf{q}}, \omega = 0) v_{cG'}(\tilde{\mathbf{q}}),$$

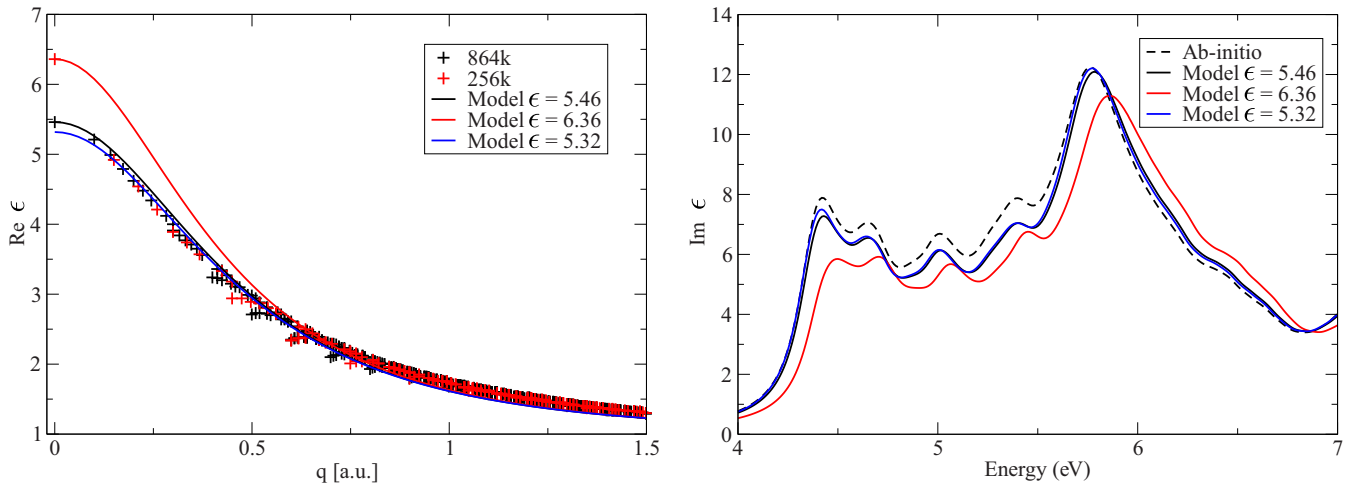


FIG. 7. Effects of the model electron-hole screening on BSE results in AgCl. Left panel: *ab initio* LDA-RPA (crosses) and model (solid lines) dielectric constants $\epsilon(\mathbf{q}, \omega = 0)$ as a function of $|\mathbf{q}|$. The *ab initio* results are obtained using four-times shifted $4 \times 4 \times 4$ (red) or $6 \times 6 \times 6$ (black) Monkhorst-Pack grids of \mathbf{k} points, corresponding to 256 or 864 \mathbf{k} points in the full Brillouin zone, respectively. The black cross at $q \rightarrow 0$ also contains the correction for the nonlocal pseudopotential, while the red cross does not. Model results are fitted to the *ab initio* results at $q = 0$ (respective color code) or at $q = 0.15$ a.u. (blue), where results on the smaller grid are already converged. Right panel: BSE spectra obtained with 864 shifted \mathbf{k} points, 8 valence and 6 conduction bands. The screening of the electron-hole interaction is taken from the results shown in the left panel: either the diagonal of the *ab initio* screened Coulomb interaction (dashed black), or the model screening fitted to the 864 \mathbf{k} points result at $q = 0$ (solid black), or to the 256 \mathbf{k} points result at $q = 0$ (red) or at $q = 0.15$ a.u. (blue).

where $\tilde{\mathbf{q}} = \mathbf{k} - \mathbf{k}'$ must correspond to the difference between two \mathbf{k} points on the grid used in the calculations. Therefore, with increasing \mathbf{k} -point grid size an increasing number of screening matrices have to be calculated. Even though the screened electron-hole interaction is calculated within the RPA and at $\omega = 0$, this quickly constitutes a formidable task, especially within the QSGW scheme.

In order to overcome this bottleneck, sometimes the *ab initio* screening is replaced by a model [107–118]. In particular, for bulk semiconductors a successful model was proposed in Ref. [119]. It represents the static dielectric function as

$$\epsilon(q) = 1 + \frac{1}{\frac{1}{\epsilon(q=0)-1} + \alpha \left(\frac{q}{q_{TF}}\right)^2 + \frac{q^4}{4\omega_p}}, \quad (12)$$

where $q_{TF} = 2(3\bar{n}/\pi)^{1/6}$ and $\omega_p = \sqrt{4\pi\bar{n}}$, with \bar{n} the average density. α is a parameter set to 1.563, following Ref. [119]. This model dielectric function only gives the diagonal in reciprocal space, but, as we will see, it is sufficient for the present purpose.

Although the model is very simple, its use requires care. First, the “average density” should not be the average density of all electrons, but only of those valence electrons that participate to the screening. This difference is well defined in a simple semiconductor such as silicon, but less obvious in materials like AgCl with electrons of different character in the valence bands. Since the model screening depends strongly on the density, comparison of the model results with various choices for the valence density to an, even not fully converged, *ab initio* calculation in a few \mathbf{q} points is sufficient to see that the screening is determined by the electrons in the eight upper valence states, i.e., the Ag $4d$ and Cl $3p$ electrons. To include some of the remaining, more tightly bound, electrons in the average density would clearly lead to overscreening.

Second, the macroscopic dielectric constant enters the model as an important parameter. Not always a reliable experimental value is known, and in a fully first-principles framework, it should be calculated. This is a much more delicate point, as we will illustrate in the following. The left panel of Fig. 7 shows the KS-RPA dielectric function $\epsilon(\mathbf{q}, \omega = 0)$, calculated with a four-times shifted $4 \times 4 \times 4$ grid of \mathbf{k} points, corresponding to 256 \mathbf{k} points in the full Brillouin zone (red crosses). This calculation yields a macroscopic dielectric constant $\epsilon(q = 0) = 6.36$. The model curve (red line) that is obtained by using this value for ϵ_0 reproduces the *ab initio* results very well at large q , and it is perfect for $q \rightarrow 0$ by definition, but for small to moderate q the discrepancy is significant. As a consequence, when the full first-principles screening of the electron-hole interaction in the BSE is replaced with this model screening, the comparison is not satisfactory, as can be seen in the right panel of Fig. 7.

Interestingly, the problem is not the model, but the *ab initio* calculations: the left panel also shows the *ab initio* results obtained with a denser Brillouin zone sampling (black crosses). The comparison highlights the fact that the value of the dielectric constant at $q = 0$ calculated on the coarse grid (red crosses) is not converged, contrary to the values obtained for nonvanishing q . Indeed, the $q = 0$ calculation should be more difficult to converge with respect to the Brillouin zone sampling: for $q \neq 0$ transition energies $\Delta\epsilon$ enter the dielectric function in a denominator, but for $q \rightarrow 0$ this denominator is determined by $(\Delta\epsilon)^3$. A second difficulty is that, unless a double \mathbf{k} grid is used, the $q \rightarrow 0$ limit requires the calculation of a correction to the dipole matrix element whenever the Hamiltonian is nonlocal [120]. This correction, which takes the form of a commutator of the potentials with the space coordinate \mathbf{r} , gives a sometimes sizable contribution in the case of nonlocal pseudopotentials, and/or when the

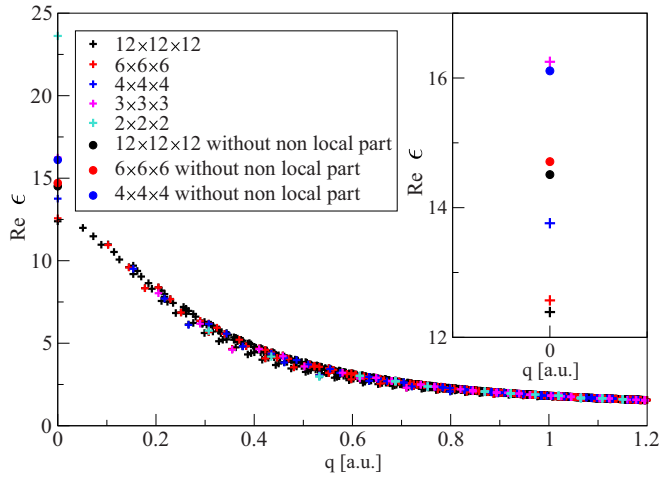


FIG. 8. Bulk silicon: Static dielectric function as function of wave vector, for different \mathbf{k} -point grid sizes. Plus (circle) symbols are results from calculations including (excluding) the commutator with the nonlocal pseudopotential. In the inset: zoom on $\mathbf{q} = 0$.

band structure stems from a nonlocal self-energy [121,122]. Both difficulties are very general and even occur in simple semiconductors such as silicon. Figure 8 gives an illustration, with $\epsilon(\mathbf{q}, \omega = 0)$ of bulk silicon shown for various grids of \mathbf{k} points, and including or excluding the commutator with the nonlocal pseudopotential. This is a Kohn-Sham calculation, so the pseudopotential is the only nonlocal component.

Since by increasing the number of \mathbf{q} points the contribution from $q = 0$ to a sum over the Brillouin zone vanishes, the poor quality of $\epsilon(q = 0)$ is often acceptable when the *ab initio* dielectric function is used in an integral, e.g., in *GW* or BSE calculations. Instead, when the macroscopic dielectric constant is used to determine the model dielectric function, a bad estimate of $\epsilon(q = 0)$ deteriorates the model screening over a large range of wave vectors, as can be seen from the left panel of Fig. 7 for AgCl, by comparing the fits obtained on the converged and unconverged *ab initio* calculations.

One might, of course, improve the calculation of the dielectric constant, but this would reduce significantly the computational gain of using the model, especially when self-consistent QP results are used (see below). Here, we propose an alternative route, namely, we fit the model to the calculated dielectric constant at a nonvanishing momentum transfer $q^0 \neq 0$. In this way, no commutator has to be evaluated, and we can make use of the fact that $\epsilon(q^0)$ converges more quickly than $\epsilon(q = 0)$. The choice of the q^0 where the model parameters should be determined is constrained: for larger q , and taking into account crystal local field effects, the local anisotropy of the crystal induces a scattering around the function $\epsilon(q)$ and therefore some arbitrariness. One therefore has to choose a value q^0 that is small enough to yield a well defined $\epsilon(q^0)$ and large enough to converge fast with the \mathbf{k} -point grid. In any case, for any $q^0 \neq 0$ the problem of the commutator is avoided. Equation (12) now turns into

$$\epsilon(q) = 1 + \frac{1}{\frac{1}{\epsilon(q^0)-1} + \alpha \frac{(q^2 - (q^0)^2)}{4\tau_F} + \frac{(q^4 - (q^0)^4)}{4\omega_p}}. \quad (13)$$

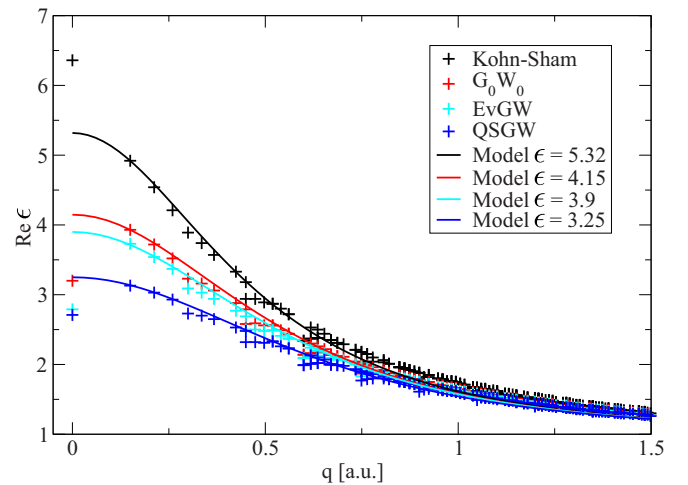


FIG. 9. Silver chloride: static dielectric constant as function of momentum transfer calculated using different levels of theory: Kohn-Sham LDA, G_0W_0 , *evQSGW*, and *QSGW*. All calculations are done using a four-times shifted $4 \times 4 \times 4$ Monkhorst-Pack \mathbf{k} -point grid and 340 bands. The commutator with the nonlocal potentials (pseudopotential and self-energy, when applicable) is neglected. The fit of the model results at $\mathbf{q}^0 = (-0.125, -0.125, 0)$ in units of the reciprocal lattice ($q = 0.15$ a.u.) yields the dielectric constants.

This approach, as we will show subsequently, is very powerful to converge optical spectra calculated from the BSE. As a byproduct, once the model parameters are determined this also allows one to extrapolate the dielectric constant at $q \rightarrow 0$. This is demonstrated in the left panel of Fig. 7: the model dielectric function obtained from the fit to the *rough* first-principles calculation at $q^0 = 0.15$ a.u. (blue curve) compares very well to the one fitted to the best first-principles calculation at $q = 0$ (black curve); from the fit at $q^0 = 0.15$ a.u. to the *unconverged* calculation, one can read an RPA dielectric constant $\epsilon(q = 0) = 5.32$, which well compares with the converged *ab initio* result $\epsilon(q = 0) = 5.46$, and which is much better than the result $\epsilon(q = 0) = 6.36$ of the unconverged *ab initio* calculation itself.

Note that the converged RPA dielectric constant of 5.46 is larger than the experimental value, which is found to lie between 3.7 [102] and 3.97 [103]. Other calculations based on KS-LDA [45] also find too large dielectric constants, similar to ours. This may be traced back to the Kohn-Sham band gap, whose influence on the dielectric constant is in the RPA not compensated by f_{xc} . However, for consistency we use the RPA value in order to simulate the RPA screening. Since over-screening leads to underestimation of the excitonic effects, we have calculated the dielectric function also using G_0W_0 , *evQSGW* and *QSGW* results as input for the RPA. Results are shown in Fig. 9. As expected, the strongest screening is obtained in the KS-RPA, the same result as presented in Fig. 7. Self-energy corrections to the eigenvalues calculated in G_0W_0 open the gap and lower the screening, with an effect that is particularly visible at smaller wave vectors. Self-consistency on the eigenvalues further opens the gap and lowers the screening, again with a stronger effect at smaller wave vectors. Self-consistency in the wave functions in *QSGW* enhances the trend, with an effect that is significant at small q , but almost

negligible above $q \approx 1$ a.u. These *ab initio* results have been obtained using a 4 times shifted $4 \times 4 \times 4$ grid, neglecting the commutator with the nonlocal pseudopotential and, in the case of the *GW* calculations, neglecting the commutator with the nonlocal self-energy. As a result, while the differences between the various approximations are significant but reasonable and smooth for $q \neq 0$, the same does not hold for $q = 0$. In particular, the dielectric constant is clearly too small when *GW* ingredients are used. The error due to the neglect of the commutator with the nonlocal self-energy is sizable, and of opposite sign with respect to the pseudopotential contribution. We therefore determine the screening at $q^0 = 0.15$ a.u., and then use Eq. (13) to obtain the full $\epsilon(q)$. This allows us to extrapolate the dielectric constants at vanishing wave vector. We obtain $\epsilon(q \rightarrow 0) = 5.32$ in Kohn-Sham as stated above, and we find 4.15 in G_0W_0 -RPA, 3.9 in *ev*QSGW+RPA, and 3.25 in QSGW+RPA, respectively. The *GW* results are therefore closer to experiment than the Kohn-Sham ones, and the help of the model in avoiding the calculation of the commutators is particularly welcome.

The quality of BSE results obtained using the model screening is shown in the right panel of Fig. 7. This picture has been obtained with 864 shifted \mathbf{k} points, for both the G_0W_0 +BSE spectra calculated with the model and with the *ab initio* screening neglecting the off-diagonal elements of screened interaction W : when the model is used in our improved procedure, the differences are very small. The intensity of the peaks is underestimated by the model screening with respect to the diagonal approximation to the *ab initio* W by an amount that is similar to the overestimation of the diagonal approximation with respect to the use of the full screening matrix $W_{GG'}(\mathbf{q})$ in the BSE (see Fig. 6). The model screening BSE calculation is therefore very close to the *ab initio* full W BSE result. We can conclude that we can safely use the model screening in order to converge the BSE spectra. Even more importantly, the model permits us to carry out the QSGW+BSE scheme for the requested dense k -point grid.

V. EXCITONS

We can now analyze the influence of the excitonic effects on the optical spectra of AgCl. We will make a detailed analysis of the character of the excitons, in order to understand their spatial localization and interpret the optical properties of AgCl.

A. Excitonic effects: Role of the screening and comparison to experiment

Figure 10 shows the absorption spectra obtained, with a converged grid of 2048 \mathbf{k} points, comparing different flavors of RPA and BSE results. All spectra are calculated with LDA wave functions. G_0W_0 +BSE and QSGW+BSE spectra differ for two reasons. First, a different scissor correction: 1.9 or 2.98 eV to simulate the G_0W_0 or QSGW band-gap opening, respectively; second, the model screening (12) is evaluated with $\epsilon_0 = 5.32$ and 3.25 for the G_0W_0 +BSE and QSGW+BSE spectra, respectively. The energy of the first exciton peak (solid lines) moves from 4.4 eV in G_0W_0 +BSE to 5.25 eV in QSGW+BSE. By comparing the BSE spectra with

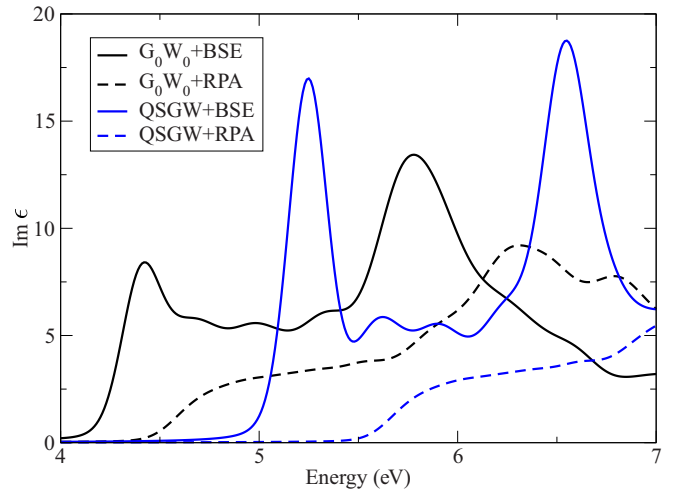


FIG. 10. Absorption spectra calculated in the RPA (dashed lines) and from the BSE (solid lines), using scissor corrections and model screenings obtained from G_0W_0 (black lines) or QSGW (blue lines).

the corresponding RPA results (dashed lines), we find that the reduced screening in QSGW+BSE crucially enhances excitonic effects with respect to G_0W_0 +BSE. The exciton binding energy for the first peak is 0.21 eV within G_0W_0 +BSE and becomes 0.43 eV within QSGW+BSE. Within the GWA the role of different approximations for the screened interaction W is well known [52,63,65,67,85,92,123–125], while it has been less investigated in the framework of BSE calculations [121,122,126–129]. In both cases, self-consistency weakens the screening, and a vertex correction would be needed to restore agreement with experiment. In the case of *GW* the absence of vertex corrections leads to too large band gaps, while in the case of BSE the effect is an increased electron-hole interaction, leading to more localized excitons. However, both in *GW* and in the BSE the overall effect of self-consistency is in general an improvement towards the experiment. This is particularly true in the BSE, where the resulting sharpening of the excitonic peaks is important and needed. It should also be noted that *GW*+BSE calculations benefit from partial error canceling since W has opposite sign in the two cases. Here we find that the larger redshift of the QSGW+BSE spectra partially compensates the larger scissor correction in the QSGW+RPA result with respect to G_0W_0 -RPA. Most importantly, however, the oscillator strength of the excitonic peak is greatly increased.

Our final results for the extinction coefficient are compared with experiment in Fig. 11. This figure, aside from the measurement at 4 K from Carrera and Brown [25] that was already presented in Sec. III C, also displays an additional experimental spectrum that we have directly converted from the absorption coefficient reported in Ueta *et al.* [31]. This spectrum, also measured at liquid-helium temperature, has the advantage of being available on a wider energy range. However, it has been obtained from the reflectivity measurement of Yanagihara *et al.* [29] using a Kramers-Kronig transformation, a procedure that introduces additional uncertainties and can lead to a large error bar in the peak intensities [130]. The two experimental spectra agree on the position of the first peak at

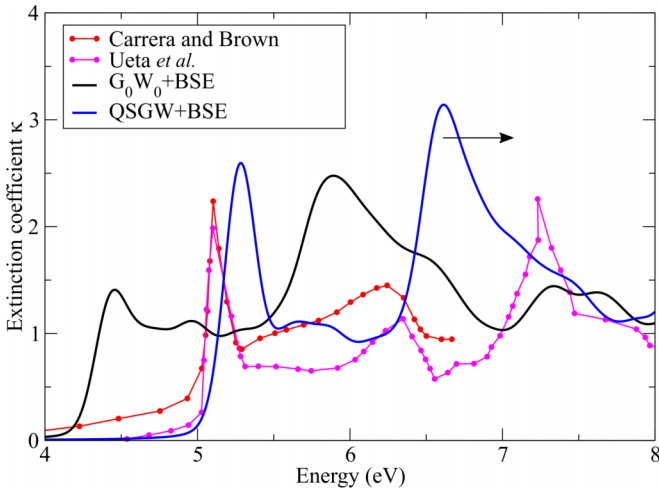


FIG. 11. Extinction coefficient spectra: comparison between experimental results [25,31], and G_0W_0 +BSE and QSGW+BSE calculations obtained with a grid of shifted 2048 \mathbf{k} points and 25 bands. The horizontal black arrow indicates the estimated shift of the 6.6-eV peak that would be obtained by using QSGW corrections instead of the scissor operator.

5.1 eV, while they show discrepancies concerning the shape of other spectral features. These differences also illustrate the limitations and the caution needed in the comparison of the calculated spectra with experiment.

The combined use of the converged \mathbf{k} -point grid and QSGW ingredients, which was made possible thanks to the model screening, improves remarkably the comparison with experiment (red line in Fig. 11) with respect to the G_0W_0 +BSE spectra (black line in Fig. 11). Further improvement might be obtained by the use of QSGW quasiparticle wave functions and by the inclusion of dynamical effects in the BSE [52], which is well beyond the scope of this work. The QSGW+BSE results (blue line) reproduce well the first sharp excitonic peak and place it very close to the experimental peak at 5.1 eV. In the calculations a Gaussian broadening of 0.09 eV accounts for the finite \mathbf{k} -point sampling and the 0.02-eV experimental resolution.² Here it is important to note that this spectral broadening does not change the area under the peaks, which can be therefore compared to the experiment. In the measured spectrum from Carrera and Brown [25] the sharp peak at 5.1 eV has a long tail extending to lower energies that has been explained in terms of phonon-assisted indirect transitions [30,31,131]. We find that the area of the calculated first peak matches well the sum of the areas of the peak and the tail in the experiment. We could therefore argue that the coupling with phonons [95,132–135], here not accounted for, could explain the transfer of spectral weight to lower energies, together with the strong temperature dependence of the measured spectra [30,31]. The spectrum by Ueta *et al.* [31], instead, does not display a similar tail at low energies: this qualitative difference between the experimental data could

be due to problems related to use of the Kramers-Kronig transformation.

The calculated BSE spectrum has a second prominent excitonic peak at 6.6 eV, which is already beyond the available energy range of the spectrum by Carrera and Brown. It should correspond to the peak at 7.2 eV in the spectrum of Ueta *et al.* The reason for the underestimation of the peak position in the calculation can be attributed to the scissor correction that becomes less accurate for larger transition energies. The independent electron-hole transitions that give rise to this excitonic peak (see Sec. VB) have QSGW corrections (see Fig. 3) that are larger by 0.4 eV than the scissor correction. By taking into account this additional shift (see black arrow in Fig. 11), the agreement between theory and experiment would be greatly improved.

In the next section we will analyze in detail the properties of these excitonic features in the spectra.

B. Analysis of the excitons

Thanks to the full diagonalization of the BSE Hamiltonian, which provides the eigenvalues E_λ and eigenvectors A_λ (see Sec. IIC), we can now analyze in detail the character of the lowest-energy excitons.

The sharp peak at the onset of the spectrum is due to three degenerate exciton states. They are not the lowest-energy excitons though: approximately 50 meV below them there is also a twofold-degenerate dark exciton that does not contribute to the absorption spectrum.

The left and middle panels of Fig. 12 represent the most important contributions to a dark and a bright exciton, respectively, in terms of electron-hole transitions in the band structure (the results for the other dark and bright excitons are similar). The size of the orange circles is proportional to the weight of $|A_\lambda^t \tilde{\rho}_t|$ contributing to the exciton λ for each vertical transition t between a valence and a conduction band at a \mathbf{k} point.

We find that these excitons originate from transitions between the top valence and the bottom conduction bands at the \mathbf{k} points close to the minimum direct gaps in the band structure. In this region, close to the Γ point, the valence and conduction bands are almost parallel, which means that many transitions of similar energy can mix and favor strong excitonic effects [136,137]. Such excitons cannot be described by simple models such as the Wannier model [138,139].

The contributions to the dark and bright excitons in the band structure look very similar. The main difference is at the Γ point, which contributes for the bright exciton, whereas it is absent for the dark exciton. The oscillator strengths for many transitions are separately not zero even for the dark exciton. In order to understand why the dark exciton has in total zero oscillator strength, one has to explicitly consider the sum over equivalent transitions in the numerator of Eq. (8), in particular over \mathbf{k} points. Indeed, for the dark excitons the BSE coefficients at $\mathbf{k} \neq 0$ are even functions of \mathbf{k} : $A_\lambda(\mathbf{k}) = A_\lambda(-\mathbf{k})$, while for the bright excitons they are odd functions: $A_\lambda(\mathbf{k}) = -A_\lambda(-\mathbf{k})$. Since for the same transitions the one-particle oscillator strengths are also odd: $\tilde{\rho}(\mathbf{k}) = -\tilde{\rho}(-\mathbf{k})$, the products $A_\lambda(\mathbf{k})\tilde{\rho}(\mathbf{k})$ interfere constructively for the bright excitons and destructively for the dark excitons. This differ-

²Additionally, a spin-orbit splitting of ~ 0.1 eV contributes to the experimental peak width [31].

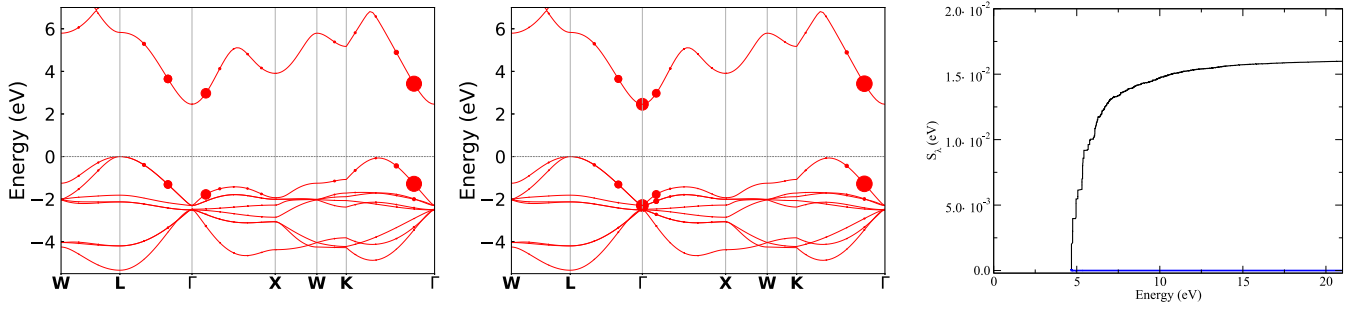


FIG. 12. (Left) Projection of $|A'_\lambda \tilde{\rho}_t\rangle$ on the band structure for one of the two dark excitons. The size of the circles is proportional to $|A'_\lambda \tilde{\rho}_t\rangle$. (Center) Same analysis for one of the three bright excitons. The scale is the same for both panels. (Right) Corresponding cumulative functions $S_\lambda(\omega)$ for the bright and dark excitons (black and blue lines, respectively).

ent mixing of formerly independent transitions is a typical manifestation of the many-body excitonic effects. The result of this constructive or destructive mixing can be seen in the right panel of Fig. 12. For the bright exciton the cumulative function $S_\lambda(\omega)$ (black line) steadily increases as a function of ω , i.e., as long as more transitions are taken into account, reaching its final intensity at around 15 eV. The picture for the dark exciton is instead very different: as a result of the cancellation between equivalent transitions at the same energy, the cumulative function $S_\lambda(\omega)$ (blue line) remains always zero, leading to the dark nature of the exciton.

We can analyze in a similar manner also the peak at 6.6 eV in the QSGW+BSE spectrum (see Fig. 11), which originates from three degenerate excitonic states λ . We explicitly consider one of these excitons in Fig. 13. From the representation of the contributions $|A'_\lambda \tilde{\rho}_t\rangle$ on the band structure in the upper panel, we can conclude that this high-energy exciton stems from electron-hole transitions distributed all over the Brillouin zone. Moreover, in contrast to the lowest-energy excitons, in this case not only transitions between the top valence and the bottom conduction bands give rise to the excitonic state, but also deeper valence bands have an important contribution.

The corresponding cumulative function, contrary to the case of the bright bound exciton in Fig. 12, is not a monotonously increasing function. To understand what happens, it is easier to look directly at $I_\lambda(\omega)$ from Eq. (11). It has a peculiar behavior: it increases when the first contributions at lower energy are summed, but it decreases shortly afterwards and becomes negative, before going up again and crossing the x axis at an energy ω_0 . After this point, it increases monotonously. This implies that the total oscillator strength of this exciton in the spectrum is given by contributions from electron-hole transitions of energy $E_t > \omega_0$. This part of the function I_λ is highlighted in orange in the bottom panel of Fig. 13. In the upper panel of the same figure, we have therefore distinguished the two kinds of contributions. Those that have an energy $E_t < \omega_0$ and do not effectively contribute to the exciton oscillator strength are represented by the black circles, while the others with energy $E_t > \omega_0$ that are sufficient to yield the final spectrum are represented by the orange circles.

In order to understand the behavior of the cumulative function in Fig. 13, it is useful to examine the excitonic eigenvector

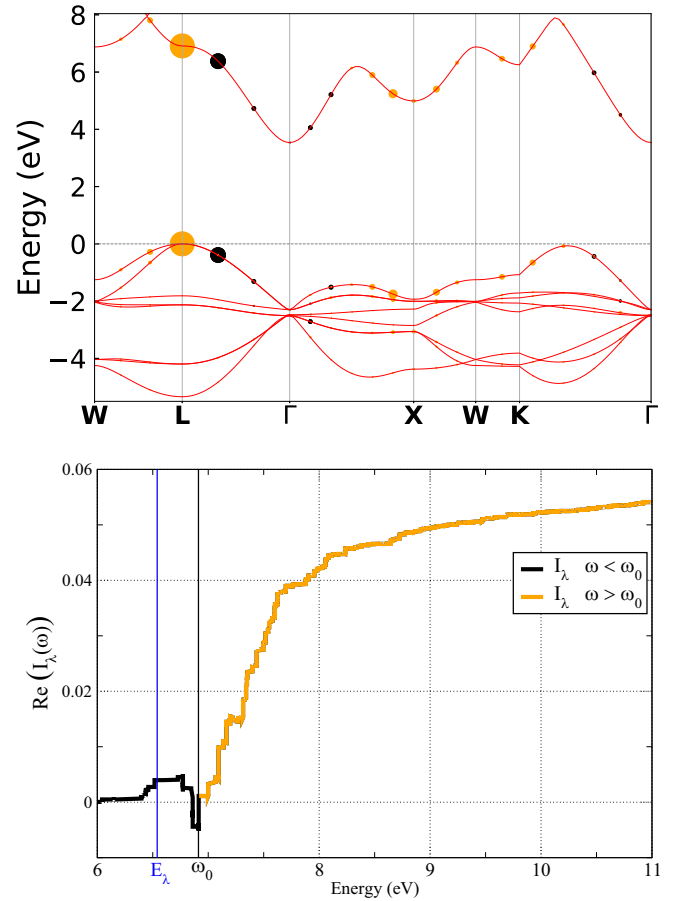


FIG. 13. (Upper panel) Projection of $|A'_\lambda \tilde{\rho}_t\rangle$ on the band structure for one of the three excitons forming the peak at 6.6 eV in the QSGW+BSE spectrum (see Fig. 11). Full black circles correspond to transition with energy smaller than the energy ω_0 given by the black vertical line in the bottom panel, full orange circles correspond to transitions at higher energy. The scale is the same as in Fig. 12. (Bottom panel) The corresponding real part of the cumulative function $I_\lambda(\omega)$ (the imaginary part, not shown, has a similar behavior). Contributions for $\omega > \omega_0$ (orange part of the curve) add constructively to form the exciton oscillator strengths, while the contributions for $\omega < \omega_0$ (in black) cancel.

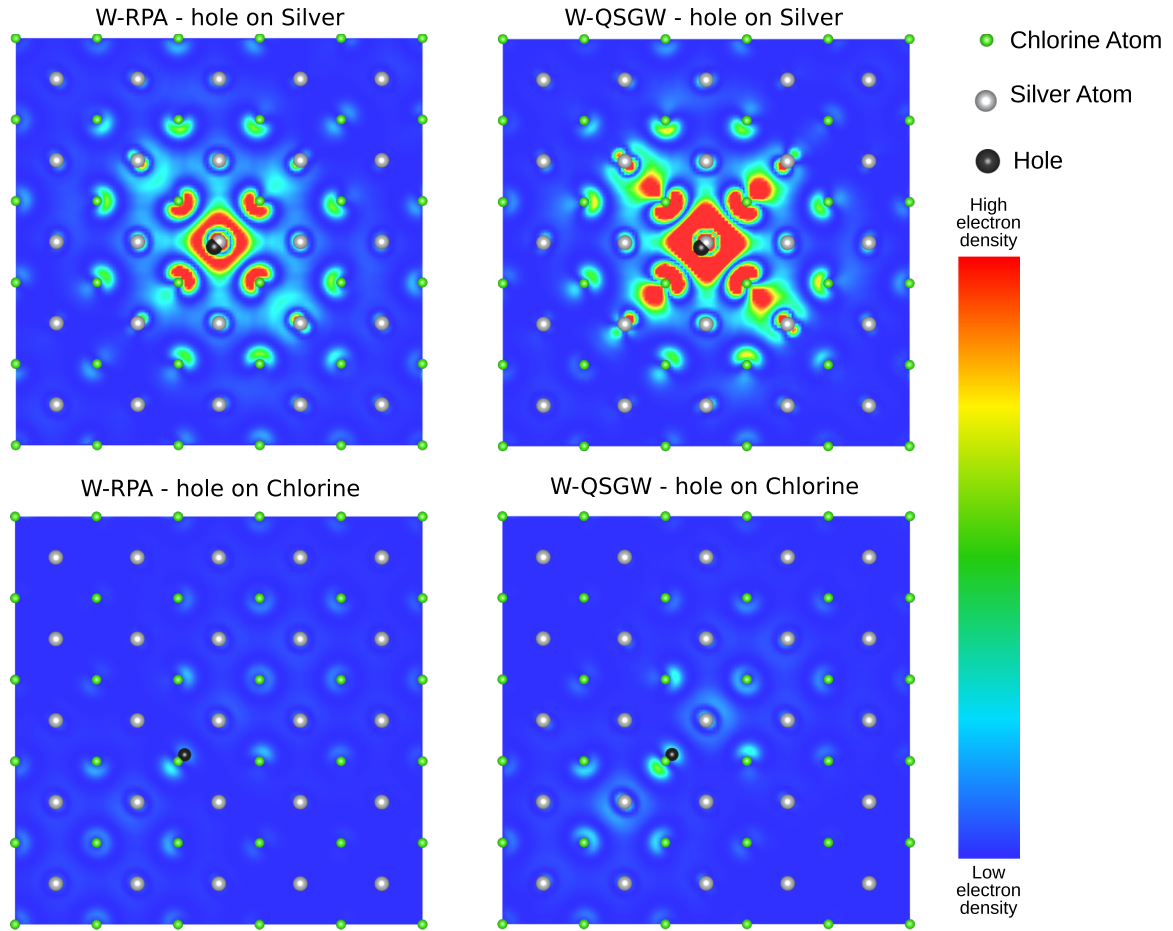


FIG. 14. Electron density distribution for the two degenerate lowest-energy dark excitons. Shown are cuts along the [101] plane for the exciton calculated in W -RPA (left panels) and W -QSGW (right panels), where the hole has been placed close to the Ag atom (top panels) and close to the Cl atom (bottom panels). Cl (Ag) atoms are represented by green (gray) balls, while the hole position is black.

A_λ to first order in K , which reads as

$$A_\lambda^t = \delta_{t,t_\lambda} + \frac{\langle t|K|t_\lambda \rangle}{E_t - E_{t_\lambda}}, \quad (14)$$

where the zero-order term is given by δ_{t,t_λ} , corresponding to the zero-order electron-hole transition t_λ within an independent particle picture. This yields

$$I_\lambda(\omega) = \sum_t^{E_t < \omega} \delta_{t,t_\lambda} \tilde{\rho}_t + \sum_t^{E_t < \omega} \frac{\langle t|K|t_\lambda \rangle}{E_t - E_{t_\lambda}} \tilde{\rho}_t + \text{BG}(\omega). \quad (15)$$

Supposing that $\tilde{\rho}_t$ does not change sign with t , the cumulative function is hence given by three contributions: (i) a steplike contribution from the zero-order term starting $\omega > E_{t_\lambda}$, (ii) the first-order term which is responsible for the non-monotonous behavior, with a negative contribution whose absolute value reaches its maximum at $\omega = E_{t_\lambda}$, and which subsequently becomes less negative and continues to increase monotonously, and (iii) a background $\text{BG}(\omega)$ due to higher orders. The sum of these terms explains the observations. Such an effect can only occur when E_{t_λ} is not among the lowest transitions energies because only for higher E_{t_λ} the sum can have negative contributions [140,141].

Finally, we examine the electron-hole correlation function $\Psi_\lambda(\mathbf{r}_h, \mathbf{r}_e)$ for the dark and bright bound excitons. Fixing the

hole at position \mathbf{r}_0 , its square modulus gives the electron probability distribution in the electron-hole pair (in each case we take the sum over the degenerate states λ). The electron-hole interaction correlates the position of the hole and the electron; it is thus necessary to compare different positions for the hole. Since the top valence band has a mixed Ag $4d$ -Cl $3p$ character, two different locations for the hole are considered: close to the Ag or the Cl sites. In order to avoid the nodes of the valence wave functions, the hole position is slightly shifted away from the atomic sites. Therefore, the electron density plots do not have the cubic symmetry of the crystal. The corresponding electron distributions are displayed in Figs. 14 and 15 in the color contour plots³ that represent a cut in the [101] plane of AgCl: the upper panels are for the hole located close to Ag atoms and the bottom panels for the hole close to the Cl atoms; the left panels correspond to calculation using $W = W_0$ from the RPA (W -RPA), while the right panels to the calculation using W from the QSGW approach (W -QSGW). The first figure shows the sum of the electron distribution for the two degenerate dark excitons and the second one the sum of the three degenerate bright excitons. The saturation

³For these plots we have used the VESTA software [142].

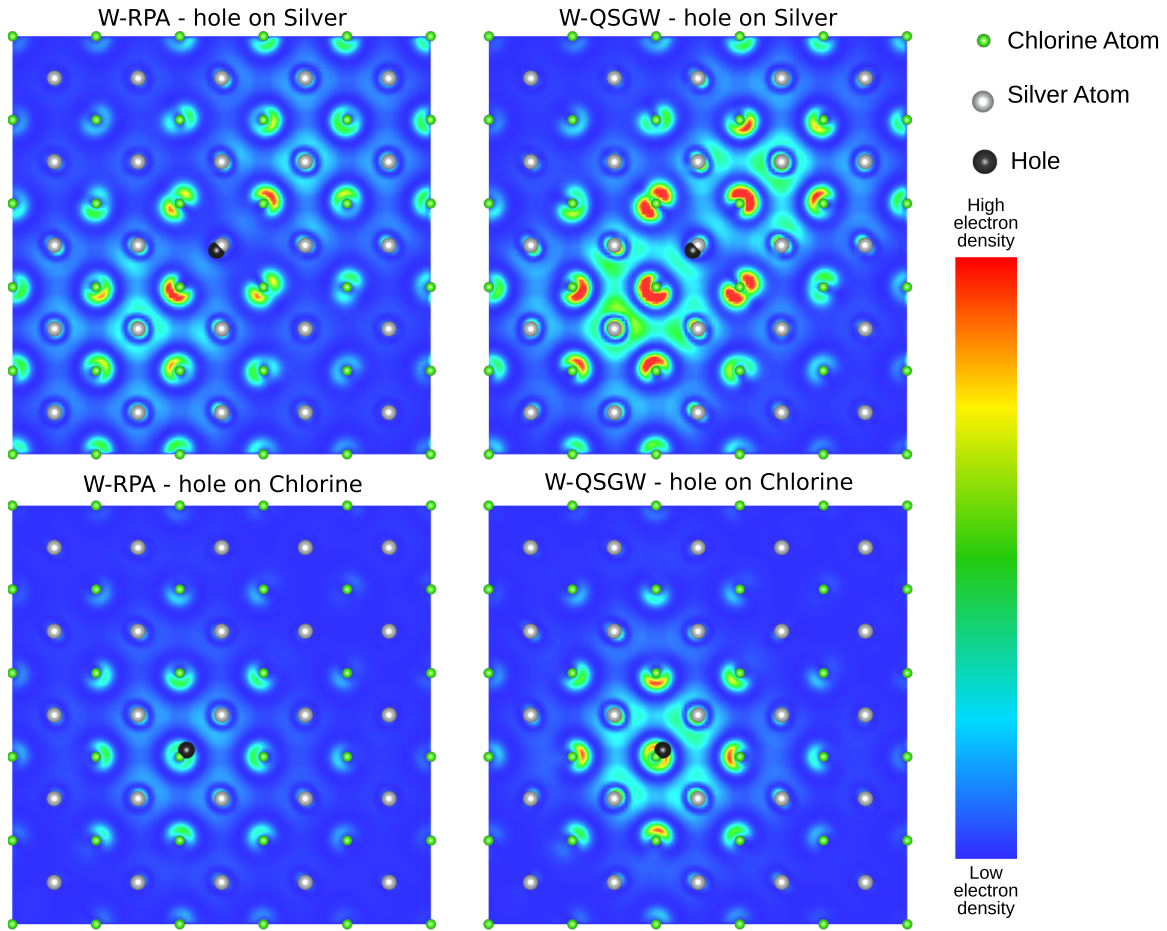


FIG. 15. Same as the previous figure for the three degenerate bright excitons.

intensity is the same in each column but it is 1.8 times larger for the dark than for the bright exciton.

The spatial distributions obtained from *W*-RPA and *W*-QSGW are qualitatively similar. However, the *W*-QSGW calculation significantly increases the electron density close to the hole, consistently with the fact that the self-consistent screening leads to a stronger electron-hole interaction.

The analysis of these plots reveals several aspects of the excitons. In both the dark and bright excitons, the intensity is stronger when the hole is placed close to silver than close to chlorine. This difference is more evident for the dark exciton than for the bright one. More importantly, the bright exciton is more delocalized than the dark exciton, whose envelope has a spatial extension that is smaller than 2 unit cells. In the bright exciton, independently on where the hole is placed, the electron density is mainly localized around chlorine atoms. It is interesting here to make a comparison with LiF, which has the same crystal structure as AgCl. Since LiF is a wide-gap insulator, one would expect a tightly bound electron-hole pair with the hole located at F sites and the electron at neighboring Li sites. BSE calculations [72,143,144] instead have shown that the electron charge is always localized on F atoms (and only weakly on Li atoms). In other words, the role of Cl in the exciton of AgCl is analogous to F in LiF.

A qualitative explanation for the electronic distribution at the atomic sites depending on the position of the hole can be

drawn from the dominant single-particle transitions that give rise to each exciton. We distinguish the two possible hole locations: if the hole is situated at a silver atom, the dark exciton is formed by the dipole-forbidden transition $\text{Ag } 3d \rightarrow 4s$, yielding a spherical shape to the electron distribution at the Ag site where the hole is located; instead, the bright exciton, thanks to the Cl-Ag hybridization of the valence band, has the character of a dipole-allowed transition $\text{Ag } d \rightarrow \text{Cl}$, giving rise to an axial electron distribution on the Cl atoms next to the hole site. If the hole is located at a chlorine atom, the dark exciton has the character of the dipole-forbidden transition $\text{Cl } 3p \rightarrow \text{Cl } 3p$ and the corresponding electron distribution at the Cl site where the hole is situated has an axial distribution; instead, the character of the bright exciton is the dipole-allowed $\text{Cl } 3p \rightarrow \text{Cl } 4s$, which is possible thanks to the fact that the Cl $4s$ contribute to the conduction band (see Fig. 2) around the Γ point where the exciton is formed. This results again in a spherical shape of the electron distribution at the Cl site where the hole is located.

VI. CONCLUSIONS

In conclusion, we have presented an extensive theoretical study of the electronic and optical properties of silver chloride, using *ab initio* calculations starting from KS-DFT. Since the KS band structure severely underestimates all gaps,

we have evaluated quasiparticle corrections using the *GW* approximation of MBPT. We have found that self-consistency is needed to produce realistic results. In order to understand the optical spectra, we had to include the electron-hole interaction, which leads to strong excitonic effects. One could in principle obtain optical spectra also from the computationally more efficient TDDFT, but excitonic effects in AgCl could not be captured by current approximations. We therefore had to solve the Bethe-Salpeter equation of MBPT.

Since convergence needs a dense Brillouin zone sampling, we used a model to describe the screening of the electron-hole interaction. The most important input for this model is the dielectric constant at vanishing wave vector, which is more difficult to determine than values at larger wave vector. We have shown that this can lead to large errors. We therefore propose to change the model input such that vanishing wave vectors can be avoided. We have shown that this leads to very good agreement between results that are calculated with the full *ab initio* screening, and those obtained using the model screening. As a byproduct, it also allows us to determine dielectric constants using different levels of theory in a very efficient way. Using this approach the agreement with experiment is improved significantly, which allows us to assign peaks and interpret the excitonic features.

The calculations show that a threefold-degenerate bright exciton, which corresponds to the strong peak that is visible at the onset in the experiment, is preceded by a twofold-degenerate exciton that is dark due to destructive interference. Analysis of the electron-hole correlation function reveals that a hole close to a silver atom leads to a strong redistribution of the electron density, whereas the effect is much weaker for a hole close to a chlorine atom. The use of a self-consistent screening calculated in QSGW strongly enhances the localization of the electron around the hole, with respect to RPA screening of the electron-hole interaction. This is interesting, as it may have consequences for the coupling of electronic excitations in AgCl to the lattice, or for the migration of charge between AgCl as a substrate and molecules adsorbed on its surface.

ACKNOWLEDGMENTS

This work was supported by a grant from the Ile-de-France Region–DIM “Matériaux anciens et patrimoniaux.” Computational time was granted by GENCI (Project No. 544). We acknowledge fruitful discussions with V. de Seauve, M.-A. Languille, and B. Lavédrine. We are thankful to V. Gorelov for the development of the analysis tool of the exciton in terms of band structure projections.

APPENDIX: COMPUTATIONAL DETAILS

We have generated Troullier-Martins [145] pseudopotentials using the FHI98PP package [146]. We used an LDA xc functional in the Perdew-Wang parametrization [147] with scalar relativistic corrections. It is generally established that spectroscopy calculations require valence shells to be complete because of the strong spatial overlap between electrons in the same shell and the consequent strong exchange effects

[126,148,149]. Here we use the slightly ionized [150] atomic configuration $1s^2 2s^2 2p^6 3s^2 3p^6 4s^2 3d^{10} 4p^6 4d^{10}$ to create the pseudopotential of silver, with the $4spd$ shell $4s^2 4p^6 4d^{10}$ in the valence. We use s as the local reference component to represent all higher angular momenta. Cutoff radii were set to 0.9 a.u. for the s , 2.3 a.u. for the p , and 1.5 a.u. for the d component, guaranteeing satisfactory logarithmic derivatives and excitation energies. Chlorine does not present the same difficulty, and we have created the pseudopotential using an atomic configuration of $1s^2 2s^2 2p^6$ for the core and $3s^2 3p^4 3d^{0.5}$ for the valence electrons. Cutoff radii were 1.6 a.u. for s and p components and 1.8 a.u. for the d component.

DFT calculations are done using the ABINIT package [151]. Converged results for AgCl were obtained by using Monkhorst-Pack [152] $8 \times 8 \times 8$ grids shifted along four directions and a kinetic energy cutoff $E_{\text{cut}} = G_{\text{max}}^2/2 = 150$ Hartree.

We have performed band-structure calculations with both G^0W^0 and QSGW, using the ABINIT package [151] and with a four-times shifted ($4 \times 4 \times 4$) grid to sample the Brillouin zone. For G^0W^0 calculations, W was obtained using 5000 plane waves to describe the wave functions and 550 bands. The size of the dielectric matrix was 1471 \mathbf{G} vectors. For the self-energy, wave functions were described with 4000 plane waves and 820 bands were used to evaluate Σ_{xc} .

For computationally heavier QSGW calculations, the basis set had to be reduced introducing an error bar of 0.2 eV with respect to fully converged G^0W^0 results. The parameters used are, for the screening, a matrix size of 1100, 340 bands, and a cutoff of 1200 plane waves for the wave functions. For the self-energy calculation, 420 bands were used as well as a cutoff of 1200 plane waves for the wave functions.

The linear-response TDDFT calculations were carried out using the DP code [153]. Convergence for both absorption and the extinction coefficient over a frequency range of 0 to 10 eV was reached using 2048 shifted \mathbf{k} points [106], 965 plane waves for the wave functions, 59 \mathbf{G} vectors for the polarizability matrix including crystal local field effects, 13 occupied bands, and 20 unoccupied bands. The spectra are calculated with a 0.1-eV Lorentzian broadening.

All BSE calculations have been performed using the EXC code [154]. As input, we use the KS band structure corrected by a scissor shift taken from our *GW* calculation. We have verified that this reproduces well the effect of the true *GW* corrections at the absorption onset but is less accurate at higher energies (see Fig. 3). We refer to G^0W^0 +BSE or QSGW+BSE for BSE calculations that use a scissor determined from G^0W^0 or QSGW band-structure calculations, respectively. The convergence with respect to the number of plane waves used to represent the KS orbitals in the BSE calculation is shown in Fig. 16. The absorption spectrum is already well converged with 965 plane waves. The BSE matrix elements are little influenced by the plane waves with large wave vector since the latter oscillate rapidly and therefore yield vanishing contributions to the matrix elements of the more slowly varying functions with which they are integrated. The convergence with respect to the number of \mathbf{k} points is illustrated by Fig. 17. The unshifted grids containing high-symmetry \mathbf{k} points converge much slower than the grids that are slightly shifted off high-symmetry \mathbf{k} points [106]. The

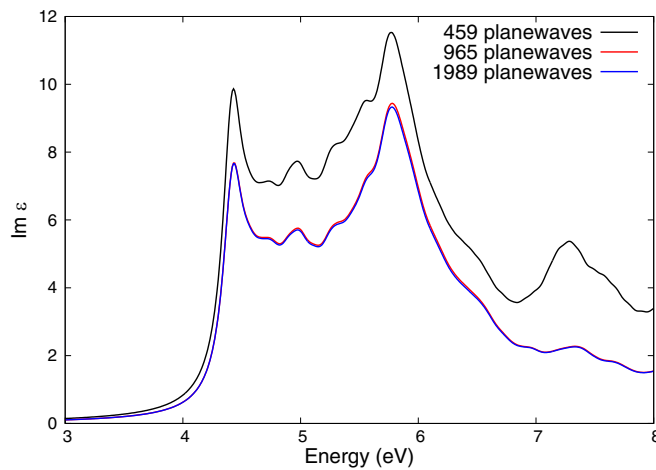


FIG. 16. Convergence of the BSE absorption spectrum with respect to the number of plane waves using a four-times shifted $8 \times 8 \times 8$ grid of \mathbf{k} points.

spectra can be considered converged with at least 2048 \mathbf{k} points.

The final G^0W^0 +BSE and QSGW+BSE spectra presented in Fig. 11 have been obtained with 0.02 Lorentzian broadening and a 0.09-eV Gaussian broadening and the following parameters: 2048 shifted \mathbf{k} points, 8 occupied and 12 unoccupied bands.

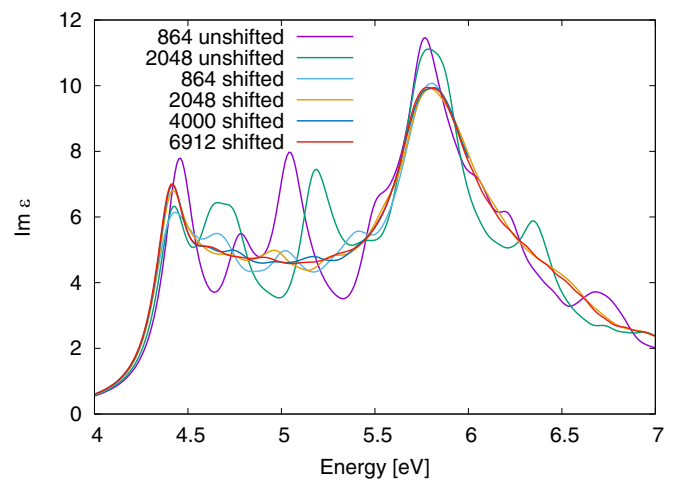


FIG. 17. Convergence of the G^0W^0 +BSE absorption spectrum as a function of the number of \mathbf{k} points in the full Brillouin zone with a 0.1-eV Lorentzian broadening.

cupied bands. To calculate these spectra we have used the Haydock iterative scheme [155,156]. For the exciton analysis, instead, we have performed a full diagonalization of the excitonic Hamiltonian using a four-time shifted $6 \times 6 \times 6$ Monkhorst-Pack \mathbf{k} -point grid, 8 occupied bands and 6 unoccupied bands.

- [1] R. G. Bates and J. MacAskill, *Pure. Appl. Chem.* **50**, 1701 (1978).
- [2] Y. Kang, J. Jung, D. Cho, O. Kwon, J. Cheon, and W. Park, *Materials (Basel)* **9**, 215 (2016).
- [3] N. D. Trinh, T. T. B. Nguyen, and T. H. Nguyen, *Adv. Nat. Sci.: Nanosci. Nanotechnol.* **6**, 045011 (2015).
- [4] A. Adams, E. Santschi, and M. Mellencamp, *Veterinary Surgery* **28**, 219 (1999).
- [5] D. Schuerch, A. Currao, S. Sarkar, G. Hodes, and G. Calzaferri, *J. Phys. Chem. B* **106**, 12764 (2002).
- [6] P. Wang, B. Huang, X. Qin, X. Zhang, Y. Dai, J. Wei, and M.-H. Whangbo, *Angew. Chem., Int. Ed.* **47**, 7931 (2008).
- [7] Z. Lou, B. Huang, P. Wang, Z. Wang, X. Qin, X. Zhang, H. Cheng, Z. Zheng, and Y. Dai, *Dalton Trans.* **40**, 4104 (2011).
- [8] X. Zhang, Y. L. Chen, R.-S. Liu, and D. P. Tsai, *Rep. Prog. Phys.* **76**, 046401 (2013).
- [9] B. Cai, J. Wang, S. Gan, D. Han, Z. Wu, and L. Niu, *J. Mater. Chem. A* **2**, 5280 (2014).
- [10] D. Jembrih-Simbürger, C. Neelmeijer, O. Schalm, P. Fredrickx, M. Schreiner, K. D. Vis, M. Mäder, D. Schryvers, and J. Caen, *J. Anal. At. Spectrom.* **17**, 321 (2002).
- [11] W. H. Armistead and S. D. Stookey, *Science* **144**, 150 (1964).
- [12] R. S. Eachus, A. P. Marchetti, and A. A. Muenter, *Annu. Rev. Phys. Chem.* **50**, 117 (1999).
- [13] C. K. Mees, *The Theory of the Photographic Process* (MacMillan, New York, 1942).
- [14] E. Becquerel, *Ann. Chim. Phys* **22**, 451 (1848).
- [15] V. de Seauve, M.-A. Languille, M. Kociak, S. Belin, J. Ablett, C. Andraud, O. Stéphan, J.-P. Rueff, E. Fonda, and B. Lavédrine, *Angew. Chem., Int. Ed.* **59**, 9113 (2020).
- [16] V. de Seauve, M.-A. Languille, S. Vanpeene, C. Andraud, C. Garnier, and B. Lavédrine, *J. Cultural Heritage* **45**, 114 (2020).
- [17] V. de Seauve, M.-A. Languille, S. Belin, J. Ablett, J.-P. Rueff, C. Andraud, N. Menguy, and B. Lavédrine, *arXiv:2001.07441*.
- [18] N. Mott and R. Gurney, *Electronic Processes in Ionic Crystals*, International Series of Monographs on Physics (Clarendon, Oxford, 1948).
- [19] F. Seitz, *Rev. Mod. Phys.* **23**, 328 (1951).
- [20] F. Moser and F. Urbach, *Phys. Rev.* **102**, 1519 (1956).
- [21] P. G. Aline, *Phys. Rev.* **105**, 406 (1957).
- [22] S. Tutihasi, *Phys. Rev.* **105**, 882 (1957).
- [23] F. Brown, T. Masumi, and H. Tippins, *J. Phys. Chem. Solids* **22**, 101 (1961).
- [24] F. C. Brown, *J. Phys. Chem.* **66**, 2368 (1962).
- [25] N. J. Carrera and F. C. Brown, *Phys. Rev. B* **4**, 3651 (1971).
- [26] P. L. Hartman and R. C. Merrill, *J. Opt. Soc. Am.* **51**, 168 (1961).
- [27] J. J. White and J. W. Straley, *J. Opt. Soc. Am.* **58**, 759 (1968).
- [28] R. S. Bauer, W. E. Spicer, and J. J. White, *J. Opt. Soc. Am.* **64**, 830 (1974).
- [29] M. Yanagihara, Y. Kondo, and H. Kanzaki, *J. Phys. Soc. Jpn.* **52**, 4397 (1983).
- [30] W. von der Osten, Excitons and exciton relaxation in silver halides, in *Polarons and Excitons in Polar Semiconductors and Ionic Crystals*, Nato ASI Subseries B, edited by J. Devreese and F. Peeters (Springer, New York, 1984), pp. 293–342.
- [31] M. Ueta, H. Kanzaki, K. Kobayashi, Y. Toyozawa, and E. Hanamura, *Excitonic Processes in Solids*, Springer Series in Solid-State Sciences (Springer, Berlin, 1986).

- [32] V. de Seauve, On the origin of colours of Edmond Becquerel's photochromatic images: A spectroscopy and electron microscopy study, Ph.D. thesis, Paris Sciences et Lettres, 2018.
- [33] X. Ma, Y. Dai, M. Guo, and B. Huang, *Chem. Phys. Chem.* **13**, 2304 (2012).
- [34] T. Benmessabih, B. Amrani, F. E. H. Hassan, F. Hamdache, and M. Zoaeter, *Phys. B* **392**, 309 (2007).
- [35] B. Amrani, F. E. H. Hassan, and M. Zoaeter, *Phys. B* **396**, 192 (2007).
- [36] A. Zaoui, M. Ferhat, and J. Hugel, *Superlattices Microstruct.* **38**, 57 (2005).
- [37] C. Okoye, *Phys. Status Solidi B* **234**, 580 (2002).
- [38] P. K. de Boer and R. A. de Groot, *J. Phys. Chem. A* **103**, 5113 (1999).
- [39] D. Vogel, P. Krüger, and J. Pollmann, *Phys. Rev. B* **58**, 3865 (1998).
- [40] P. Hohenberg and W. Kohn, *Phys. Rev.* **136**, B864 (1964).
- [41] W. Kohn and L. J. Sham, *Phys. Rev.* **140**, A1133 (1965).
- [42] L. Hedin, *Phys. Rev.* **139**, A796 (1965).
- [43] A. L. Fetter and J. D. Walecka, *Quantum Theory of Many-particle Systems* (McGraw-Hill, New York, 1971).
- [44] M. J. van Setten, M. Giantomassi, X. Gonze, G.-M. Rignanese, and G. Hautier, *Phys. Rev. B* **96**, 155207 (2017).
- [45] W. Gao, W. Xia, Y. Wu, W. Ren, X. Gao, and P. Zhang, *Phys. Rev. B* **98**, 045108 (2018).
- [46] M.-Y. Zhang and H. Jiang, *Phys. Rev. B* **100**, 205123 (2019).
- [47] F. Bassani, R. S. Knox, and W. B. Fowler, *Phys. Rev.* **137**, A1217 (1965).
- [48] J. S.-Y. Wang, M. Schlüter, and M. L. Cohen, *Phys. Status Solidi B* **77**, 295 (1976).
- [49] G. Onida, L. Reining, and A. Rubio, *Rev. Mod. Phys.* **74**, 601 (2002).
- [50] E. Runge and E. K. U. Gross, *Phys. Rev. Lett.* **52**, 997 (1984).
- [51] C. Ullrich, *Time-dependent Density-functional Theory: Concepts and Applications*, Oxford Graduate Texts (Oxford University Press, Oxford, 2012).
- [52] R. Martin, L. Reining, and D. Ceperley, *Interacting Electrons: Theory and Computational Approaches* (Cambridge University Press, Cambridge, 2016).
- [53] E. E. Salpeter and H. A. Bethe, *Phys. Rev.* **84**, 1232 (1951).
- [54] G. Strinati, *Riv. Nuovo Cimento* **11**, 1 (1988), and references therein.
- [55] M. Petersilka, U. J. Gossmann, and E. K. U. Gross, *Phys. Rev. Lett.* **76**, 1212 (1996).
- [56] S. L. Adler, *Phys. Rev.* **126**, 413 (1962).
- [57] N. Wiser, *Phys. Rev.* **129**, 62 (1963).
- [58] R. Del Sole and R. Girlanda, *Phys. Rev. B* **48**, 11789 (1993).
- [59] M. S. Hybertsen and S. G. Louie, *Phys. Rev. B* **34**, 5390 (1986).
- [60] R. W. Godby, M. Schlüter, and L. J. Sham, *Phys. Rev. B* **37**, 10159 (1988).
- [61] F. Aryasetiawan and O. Gunnarsson, *Rep. Prog. Phys.* **61**, 237 (1998).
- [62] W. G. Aulbur, L. Jönsson, and J. W. Wilkins, *Solid State Phys.* **54**, 1 (2000).
- [63] F. Bechstedt, *Many-Body Approach to Electronic Excitations: Concepts and Applications*, Springer Series in Solid-State Sciences (Springer, Berlin, 2014).
- [64] S. V. Faleev, M. van Schilfhaarde, and T. Kotani, *Phys. Rev. Lett.* **93**, 126406 (2004).
- [65] M. van Schilfhaarde, T. Kotani, and S. Faleev, *Phys. Rev. Lett.* **96**, 226402 (2006).
- [66] F. Bruneval, N. Vast, and L. Reining, *Phys. Rev. B* **74**, 045102 (2006).
- [67] F. Bruneval and M. Gatti, *Top. Curr. Chem.* **347**, 99 (2014).
- [68] R. W. Godby and R. J. Needs, *Phys. Rev. Lett.* **62**, 1169 (1989).
- [69] S. Lebègue, B. Arnaud, M. Alouani, and P. E. Bloechl, *Phys. Rev. B* **67**, 155208 (2003).
- [70] W. Hanke and L. J. Sham, *Phys. Rev. Lett.* **43**, 387 (1979).
- [71] S. Albrecht, L. Reining, R. Del Sole, and G. Onida, *Phys. Rev. Lett.* **80**, 4510 (1998).
- [72] M. Rohlfing and S. G. Louie, *Phys. Rev. B* **62**, 4927 (2000).
- [73] I. Tamm, *J. Phys. (USSR)* **9**, 449 (1945).
- [74] S. M. Dancoff, *Phys. Rev.* **78**, 382 (1950).
- [75] C. R. Berry, *Phys. Rev.* **97**, 676 (1955).
- [76] S. Hull and D. A. Keen, *Phys. Rev. B* **59**, 750 (1999).
- [77] K. Nakamura and W. von der Osten, *J. Phys. C: Solid State Phys.* **16**, 6669 (1983).
- [78] J. Tejada, N. J. Shevchik, W. Braun, A. Goldmann, and M. Cardona, *Phys. Rev. B* **12**, 1557 (1975).
- [79] A. B. Kunz, *Phys. Rev. B* **26**, 2070 (1982).
- [80] M. G. Mason, *Phys. Rev. B* **11**, 5094 (1975).
- [81] J. Yeh and I. Lindau, *At. Data Nucl. Data Tables* **32**, 1 (1985).
- [82] S.-H. Wei and A. Zunger, *Phys. Rev. B* **37**, 8958 (1988).
- [83] T. Kotani, M. van Schilfhaarde, and S. V. Faleev, *Phys. Rev. B* **76**, 165106 (2007).
- [84] N. E. Christensen, A. Svane, R. Laskowski, B. Palanivel, P. Modak, A. N. Chantis, M. van Schilfhaarde, and T. Kotani, *Phys. Rev. B* **81**, 045203 (2010).
- [85] A. Svane, N. E. Christensen, M. Cardona, A. N. Chantis, M. van Schilfhaarde, and T. Kotani, *Phys. Rev. B* **84**, 205205 (2011).
- [86] A. Grüneis, G. Kresse, Y. Hinuma, and F. Oba, *Phys. Rev. Lett.* **112**, 096401 (2014).
- [87] B.-C. Shih, Y. Xue, P. Zhang, M. L. Cohen, and S. G. Louie, *Phys. Rev. Lett.* **105**, 146401 (2010).
- [88] C. Friedrich, M. C. Müller, and S. Blügel, *Phys. Rev. B* **83**, 081101(R) (2011).
- [89] M. Stankovski, G. Antonius, D. Waroquiers, A. Miglio, H. Dixit, K. Sankaran, M. Giantomassi, X. Gonze, M. Côté, and G.-M. Rignanese, *Phys. Rev. B* **84**, 241201(R) (2011).
- [90] W. Kang and M. S. Hybertsen, *Phys. Rev. B* **82**, 085203 (2010).
- [91] J. A. Berger, L. Reining, and F. Sottile, *Phys. Rev. B* **82**, 041103(R) (2010).
- [92] M. Shishkin, M. Marsman, and G. Kresse, *Phys. Rev. Lett.* **99**, 246403 (2007).
- [93] F. Giustino, S. G. Louie, and M. L. Cohen, *Phys. Rev. Lett.* **105**, 265501 (2010).
- [94] E. Cannuccia and A. Marini, *Phys. Rev. Lett.* **107**, 255501 (2011).
- [95] F. Giustino, *Rev. Mod. Phys.* **89**, 015003 (2017).
- [96] A. Miglio, V. Brousseau-Couture, E. Godbout, G. Antonius, Y.-H. Chan, S. G. Louie, M. CÃté, M. Giantomassi, and X. Gonze, *npj Comput. Mater.* **6**, 167 (2020).
- [97] P. Ghosez, X. Gonze, and R. W. Godby, *Phys. Rev. B* **56**, 12811 (1997).

- [98] L. Reining, V. Olevano, A. Rubio, and G. Onida, *Phys. Rev. Lett.* **88**, 066404 (2002).
- [99] S. Botti, F. Sottile, N. Vast, V. Olevano, L. Reining, H.-C. Weissker, A. Rubio, G. Onida, R. Del Sole, and R. W. Godby, *Phys. Rev. B* **69**, 155112 (2004).
- [100] P. E. Trevisanutto, A. Terentjevs, L. A. Constantin, V. Olevano, and F. D. Sala, *Phys. Rev. B* **87**, 205143 (2013).
- [101] M. Hellgren and E. K. U. Gross, *Phys. Rev. A* **88**, 052507 (2013).
- [102] K. Wakamura, M. Sugioka, K. Kawakami, and M. Kurita, *Phys. B (Amsterdam)* **219-220**, 457 (1996).
- [103] R. P. Lowndes, *Phys. Rev. B* **6**, 4667 (1972).
- [104] S. Sharma, J. K. Dewhurst, A. Sanna, and E. K. U. Gross, *Phys. Rev. Lett.* **107**, 186401 (2011).
- [105] S. Rigamonti, S. Botti, V. Veniard, C. Draxl, L. Reining, and F. Sottile, *Phys. Rev. Lett.* **114**, 146402 (2015).
- [106] L. X. Benedict, E. L. Shirley, and R. B. Bohn, *Phys. Rev. Lett.* **80**, 4514 (1998).
- [107] B. I. Lundqvist, *Phys. Kondens. Mater.* **6**, 206 (1967).
- [108] D. L. Johnson, *Phys. Rev. B* **9**, 4475 (1974).
- [109] Z. H. Levine and S. G. Louie, *Phys. Rev. B* **25**, 6310 (1982).
- [110] F. Bechstedt, M. Fiedler, C. Kress, and R. Del Sole, *Solid State Commun.* **89**, 669 (1994).
- [111] E. L. Shirley, *Ultramicroscopy* **106**, 986 (2006).
- [112] M. Rohlfing, *Phys. Rev. B* **82**, 205127 (2010).
- [113] A. Tal, P. Liu, G. Kresse, and A. Pasquarello, *Phys. Rev. Research* **2**, 032019(R) (2020).
- [114] J. Vinson and E. L. Shirley, *Phys. Rev. B* **103**, 245143 (2021).
- [115] L. V. Keldysh, *Pis'ma Zh. Eksp. Teor. Fiz.* **29**, 716 (1979) [*JETP Lett.* **29**, 658 (1979)].
- [116] P. Cudazzo, I. V. Tokatly, and A. Rubio, *Phys. Rev. B* **84**, 085406 (2011).
- [117] S. Latini, T. Olsen, and K. S. Thygesen, *Phys. Rev. B* **92**, 245123 (2015).
- [118] M. L. Trolle, T. G. Pedersen, and V. Veniard, *Sci. Rep.* **7**, 39844 (2017).
- [119] G. Cappellini, R. Del Sole, L. Reining, and F. Bechstedt, *Phys. Rev. B* **47**, 9892 (1993).
- [120] S. Baroni and R. Resta, *Phys. Rev. B* **33**, 7017 (1986).
- [121] S. Körbel, D. Kammerlander, R. Sarmiento-Pérez, C. Attaccalite, M. A. L. Marques, and S. Botti, *Phys. Rev. B* **91**, 075134 (2015).
- [122] M. Gatti, F. Sottile, and L. Reining, *Phys. Rev. B* **91**, 195137 (2015).
- [123] M. Shishkin and G. Kresse, *Phys. Rev. B* **75**, 235102 (2007).
- [124] W. Chen and A. Pasquarello, *Phys. Rev. B* **92**, 041115(R) (2015).
- [125] F. Caruso, M. Dauth, M. J. van Setten, and P. Rinke, *J. Chem. Theory Comput.* **12**, 5076 (2016).
- [126] F. Bruneval, N. Vast, L. Reining, M. Izquierdo, F. Sirotti, and N. Barrett, *Phys. Rev. Lett.* **97**, 267601 (2006).
- [127] F. Bruneval, S. M. Hamed, and J. B. Neaton, *J. Chem. Phys.* **142**, 244101 (2015).
- [128] D. Jacquemin, I. Duchemin, and X. Blase, *J. Chem. Theory Comput.* **11**, 3290 (2015).
- [129] B. Cunningham, M. Grüning, P. Azarhoosh, D. Pashov, and M. van Schilfgaarde, *Phys. Rev. Materials* **2**, 034603 (2018).
- [130] H.-C. Weissker, J. Serrano, S. Huotari, E. Luppi, M. Cazzaniga, F. Bruneval, F. Sottile, G. Monaco, V. Olevano, and L. Reining, *Phys. Rev. B* **81**, 085104 (2010).
- [131] K. Song and R. Williams, *Self-Trapped Excitons*, Springer Series in Solid-State Sciences (Springer, Berlin, 2013).
- [132] A. Marini, *Phys. Rev. Lett.* **101**, 106405 (2008).
- [133] J. Noffsinger, E. Kioupakis, C. G. Van de Walle, S. G. Louie, and M. L. Cohen, *Phys. Rev. Lett.* **108**, 167402 (2012).
- [134] M. Zacharias, C. E. Patrick, and F. Giustino, *Phys. Rev. Lett.* **115**, 177401 (2015).
- [135] P. Cudazzo, *Phys. Rev. B* **102**, 045136 (2020).
- [136] H. Ehrenreich, H. R. Philipp, and B. Segall, *Phys. Rev.* **132**, 1918 (1963).
- [137] W. A. Harrison, *Phys. Rev.* **147**, 467 (1966).
- [138] R. S. Knox, *Theory of Excitons* (Academic, New York, 1963).
- [139] F. Bassani and G. P. Parravicini, *Electronic States and Optical Transitions in Solids* (Pergamon, New York, 1975).
- [140] L. Yang, J. Deslippe, C.-H. Park, M. L. Cohen, and S. G. Louie, *Phys. Rev. Lett.* **103**, 186802 (2009).
- [141] L. Sponza, V. Vénard, F. Sottile, C. Giorgetti, and L. Reining, *Phys. Rev. B* **87**, 235102 (2013).
- [142] K. Momma and F. Izumi, *J. Appl. Crystallogr.* **44**, 1272 (2011).
- [143] M. Rohlfing and S. G. Louie, *Phys. Rev. Lett.* **81**, 2312 (1998).
- [144] M. Gatti and F. Sottile, *Phys. Rev. B* **88**, 155113 (2013).
- [145] N. Troullier and J. L. Martins, *Phys. Rev. B* **43**, 1993 (1991).
- [146] M. Fuchs and M. Scheffler, *Comput. Phys. Commun.* **119**, 67 (1999).
- [147] J. P. Perdew and Y. Wang, *Phys. Rev. B* **45**, 13244 (1992).
- [148] M. Rohlfing, P. Krüger, and J. Pollmann, *Phys. Rev. Lett.* **75**, 3489 (1995).
- [149] A. Marini, G. Onida, and R. Del Sole, *Phys. Rev. Lett.* **88**, 016403 (2001).
- [150] G. B. Bachelet, D. R. Hamann, and M. Schlüter, *Phys. Rev. B* **26**, 4199 (1982).
- [151] X. Gonze, G.-M. Rignanese, M. Verstraete, J.-M. Beuken, Y. Pouillon, R. Caracas, F. Jollet, M. Torrent, G. Zerah, M. Mikami *et al.*, *Z. Kristallogr.* **220**, 558 (2005).
- [152] H. J. Monkhorst and J. D. Pack, *Phys. Rev. B* **13**, 5188 (1976).
- [153] F. Sottile, L. Reining, and V. Olevano, The DP code, https://etsf.polytechnique.fr/software/Ab_Initio/.
- [154] L. Reining, V. Olevano, F. Sottile, S. Albrecht, and G. Onida, The EXC code, https://etsf.polytechnique.fr/software/Ab_Initio/.
- [155] R. Haydock, *Comput. Phys. Commun.* **20**, 11 (1980).
- [156] L. X. Benedict, E. L. Shirley, and R. B. Bohn, *Phys. Rev. B* **57**, R9385(R) (1998).